KRONOS FUSION ENERGY

PAPER 2.11 · THE KRONOS 2026 SERIES

Bootstrap-Aligned Steady-State Current Sustainment Without a Central Solenoid: NBCD, ECCD and LHCD for a Compact Spherical-Tokamak Breeder

A compact breeder that runs continuously has no inductive transformer to renew its plasma current: the full current must be held by the self-generated neoclassical bootstrap...

Read it live — 3-D model · physics validator · film series

BY P I FORD AND G L KULCINSKI

2026 · EDITORIAL EDITION

THE OFFICIAL RECORD

What this document is, and how to read its numbers

This is a combined editorial. It gathers, in one volume, the two design studies Kronos Fusion Energy released in 2026 — a compact spherical-tokamak tritium/helium-3 breeder and a deuterium–helium-3 tandem-mirror generator — together with the intellectual-property estate, the people, and, in the internal edition, the full commercial case. The scientific text is the same text that appears in the arXiv preprints and the journal submissions; the editorial adds the apparatus a reader needs to hold the whole program at once, and nothing in the physics is altered to fit it.

THE HONESTY STANCE IS THE ASSET

Every headline quantity carries an **evidence class** — DERIVED RECOMPUTED MEASURED REQUIREMENT — and, where a number is a modelled extrapolation rather than a demonstrated value, it is labelled as such and its downside is shown next to it. Several quantities in the underlying corpus moved after first publication; where a value has been withdrawn or restated, the record says so plainly. This is deliberate: a diligence team will find the load-bearing assumptions, so the document surfaces them first.

TWO EDITIONS

This volume is issued in two editions. The **public edition** (light) carries the physics and the design only — no dollar, price, or per-kilogram figure appears anywhere in it. The **internal edition** (dark) adds the economics, the funding architecture, and the defense-commercial analysis, and is marked *Confidential* accordingly; it is not for public distribution. Where the commercial case rests on a modelled assumption rather than a demonstrated one, it is labelled as such and its downside is shown alongside it, on the same terms as the physics.

TITLE	The Kronos Fleet — Hyperion · Aegis · MetroVolt: A Combined Design & Commercialization Study
AUTHOR	Priyanca Ford, Founder & CEO, on behalf of Kronos Fusion Energy
EDITION	2026 Combined Editorial · first issue
COMPANION WORKS	The five-paper arXiv drop — (1) Breeder, (2) Burner, (3) REBCO magnet & tape, (4) Direct Energy Conversion, (5) AI/ML/Quantum control — with matching numbered Zenodo deposits, plus the IOP journal and IAEA-FEC submissions. Patents were filed before the drop.
NAMING	Hyperion = the breeder; Aegis (defense) and MetroVolt (data-center) = one generator in two housings. Internal mode letters (D1, L) do not appear on public surfaces.
STATUS	Conceptual design & simulation study. Nothing herein is a construction commitment.

HOW TO READ THIS VOLUME

The fleet at a glance, and the way its numbers are marked

This volume opens with *Orientation*, presents the five research papers as a bound sequence, and closes with the *Apparatus*. *Foundations* sets out the three general results both machines rest on. *Paper One* is the Hyperion breeder; *Paper Two* the Aegis / MetroVolt generator; *Papers Three, Four and Five* are the enabling science — high-field REBCO magnets and tape, direct energy conversion, and the AI / ML / quantum control stack. A *Digital Twin & 3-D Model* part follows, then the *Environmental* profile. The *Economics* and levelized cost and the *Business Case* and diligence record appear in the internal edition only; the *Simulations* proof record and the Apparatus — patent portfolio, team, limitations, and sources — close both editions.

THE FLEET AT A GLANCE

	HYPERION	AEGIS	METROVOLT
Role	Strategic-isotope foundry	Defense installation power	Campus power
Machine	**Spherical tokamak**	**Tandem mirror**	**Tandem mirror**
Fuel	Deuterium–tritium	Deuterium–helium-3	Deuterium–helium-3
Delivers	Tritium · ^{3}He · 14 MeV n	Resilient installation power	Firm campus power
Physics bar	**Fusion gain only**	Closure (gates named)	Closure + lunar ^{3}He
In the fleet	Breeds the fuel	Proves the generator	Commercial destination

HOW THE NUMBERS ARE MARKED

Every headline quantity carries an evidence class — DERIVED from first principles, RECOMPUTED from raw data, MEASURED in hardware, or a REQUIREMENT yet to be met. Financial figures carry a case label and are confined to the internal (confidential) edition. Values that moved after first publication are shown as withdrawn or restated rather than quietly changed. A capability you can evaluate is one whose limits are on the page.

ABSTRACT

Bootstrap-Aligned Steady-State Current Sustainment Without a Central Solenoid: NBCD, ECCD and LHCD for a Compact Spherical-Tokamak Breeder

A compact breeder that runs continuously has no inductive transformer to renew its plasma current: the full current must be held by the self-generated neoclassical bootstrap current plus external non-inductive drive, and the power that drive consumes is a real, named charge against the platform. We formalise and close the steady-state current balance for the Hyperion breeder at its frozen operating point ($I_p = 9.66\,MA$, $Q = 3.076$, $P_{\text{fus}} = 85.04\,MW$, negative triangularity $\delta = -0.30$, $B_0 = 8\,T$, elongation $\kappa = 2.0$, major radius $R_0 = 1.20\,m$, aspect ratio $A = 2.5$, centrepost peak field $16.84\,T$). Starting from the flux-surface-averaged parallel Ohm's law and the poloidal-flux diffusion equation, we reduce the sustainment problem to a per-surface current balance and evaluate the bootstrap term two ways: with the Sauter analytic closure and with a first-principles drift-kinetic (NEO) calculation carrying the full linearised Fokker–Planck collision operator. The bootstrap fraction is deliberately modest — $f_{\text{bs}} = 0.155$, i.e. $1.50\,MA$ of the $9.66\,MA$ total — because a spherical tokamak carries a large current at low poloidal beta ($\beta_p \simeq 0.25$, consistent with the Peng–Strickler ST scaling), so despite a large $\sqrt{\varepsilon}$ the device is current-drive-dominated rather than bootstrap-dominated. The remaining $8.16\,MA$ is supplied non-inductively, which the frozen design books at $118.5\,MW$ of neutral-beam current drive, an aggregate engineering efficiency of $\gamma_{\text{CD}} = \bar{n}_{e,20} R_0 I_{\text{CD}} / P_{\text{CD}} = 0.33 \times 10^{20}\ \text{A W}^{-1}\,\text{m}^{-2}$. The first-principles NEO calculation reproduces the known Sauter over-prediction at low collisionality, giving NEO/Sauter parallel-current ratios of $0.811/0.843/0.873$ at $r/a = 0.5/0.6/0.7$ ($\nu_e^* \simeq 0.012$, banana regime). Because the device is current-drive-dominated, the residual uncertainty in the bootstrap *magnitude* maps to only a bounded ($\sim 10\%$) change in the drive power and never to a loss of sustainment. The plasma self-supplies its $\simeq 19.6\,weber$ of poloidal flux ($L_p \simeq 2.03$ Henry)*withnocentralsolenoid*, *andacurrent − drive − limitedrampreaches flat − topin*\!43 s(\!3$ resistive times). Every headline number is a frozen anchor in the Kronos Physics De-Risking Register. The single open item is a full-profile drift-kinetic confirmation of the bootstrap *amplitude*; we state it plainly and show why the platform does not hinge on it.

Open-access deposit (code & data, CC BY 4.0): DOI 10.5281/zenodo.22645758 · Zenodo community *kronos_fusion_energy*. Explore it live: interactive 3-D model · physics validator.

Keywords: bootstrap current · non-inductive current drive · NBCD · ECCD · LHCD · solenoid-free operation · spherical-tokamak breeder

CONTENTS

Table of Contents

NOMENCLATURE

Symbols, units, and the names of things

Q	plasma (fusion) gain, P_{fus}/P_{aux}
Q_E	engineering gain, net electric out / recirculating in
H_{98}	confinement enhancement over the IPB98(y,2) scaling
Z_{eff}	effective ion charge
c_{ee}	electron–electron bremsstrahlung leading coefficient, 2.120022 (exact)
τ_E	energy confinement time
I_p	plasma current
R_0, a	major radius, minor radius
κ, δ	elongation, triangularity
β_N	normalized plasma beta (Troyon-normalized)
TBR	tritium breeding ratio
DEC	direct energy conversion
CF	plant capacity factor (availability)
FOAK / NOAK / BOAK	first / nth / best of a kind
Hyperion	the ST breeder (internal: Mode D2)
Aegis	the generator, defense/installation housing (internal: Mode M)
MetroVolt	the generator, data-center housing (Mode M)

bootstrap current; non-inductive current drive; NBCD; ECCD; LHCD; solenoid-free operation; spherical-tokamak breeder

§ 1

Introduction

STEADY STATE MEANS NO TRANSFORMER

An inductively driven tokamak sustains its toroidal plasma current by transformer action: a changing poloidal flux through the central solenoid induces a toroidal loop voltage. That flux is finite, so purely inductive operation is inherently pulsed. A *breeder* whose product is tritium, helium-3 and a steady 14 MeV neutron output cannot be pulsed on the transformer's schedule; it must run continuously, which means the plasma current has to be renewed without an inductive electric field. Two mechanisms remain: the plasma's own pressure-driven *bootstrap* current [1,2,3], and *external* non-inductive current drive by neutral beams or radio-frequency waves [4,5]. The bootstrap current is free; the external share costs recirculating power. An honest steady-state design states that cost as a named line rather than assuming it away behind an optimistically high bootstrap fraction.

For a compact spherical tokamak (ST) the balance has a particular character. The ST carries a large plasma current in a small volume at low aspect ratio, which is exactly what makes it an attractive neutron source and breeder platform [6,7,8,28], and at the same time it fixes the poloidal beta at a modest value. The bootstrap fraction, which scales as $f_{\rm bs} \simeq c_{\rm bs}\sqrt{\varepsilon}\,\beta_p$, therefore comes out *modest* despite the large inverse aspect ratio $\varepsilon = a/R_0$: the large $\sqrt{\varepsilon}$ is multiplied by a small β_p. This is the opposite regime from the high-β_p steady-state reactor concept in which the bootstrap current supplies 70%–100% of the total [9]. The Hyperion breeder is *current-drive-dominated*, and the design task is to size and shape that drive.

THE SPHERICAL TOKAMAK'S CURRENT-DRIVE PROBLEM, QUANTITATIVELY

At the frozen operating point the plasma current is $I_p = 9.66\,MA$ (register serial BR-L1-A7, $Q = 3.076$, $P_{\rm fus} = 85.04\,MW$). The bootstrap current self-generated by the pressure gradient is $I_{\rm bs} = 1.50\,MA$, a fraction $f_{\rm bs} = 0.155$ (BR-L2-A6). The residual $I_{\rm cd} = I_p - I_{\rm bs} = 8.16\,MA$ must be driven non-inductively. Because this residual is large, current-drive *power* — not bootstrap alignment — is the load-bearing constraint: with $f_{\rm bs}$ only 0.155, the safety-factor profile is set mainly by where the external current is deposited, so bootstrap misalignment is a minor concern here, and the real risk the design must retire is the availability and efficiency of the drive. The purpose of this paper is to write that balance down from first principles, evaluate the bootstrap term with a drift-kinetic code, size the drive mix, and bound the sensitivity of the answer.

PRIOR ART

The neoclassical bootstrap current has an accurate analytic closure valid across collisionality regimes — the Sauter–Angioni–Lin-Liu formulae [10,11], refined more recently by Redl *et al.* [12] and, for the steep edge, by kinetic calculations [13]. First-principles evaluation is provided by drift-kinetic solvers with the full linearised Fokker–Planck operator, of which NEO is the reference [14,15]. External current drive rests on the theory of Fisch and co-workers [4,16]: neutral-beam current drive (NBCD) with the trapped-electron shielding correction of Lin-Liu and Hinton [17,18]; electron-cyclotron current drive (ECCD) by the Fisch–Boozer and Ohkawa mechanisms [19]; and lower-hybrid current drive (LHCD), the most efficient but accessibility-limited option [20]. The integrated steady-state picture for conventional aspect ratio is laid out in the ITER Physics Basis [5] and realised in real-time profile simulators [23]. What is specific to the compact ST breeder, and what we supply here, is the *closed, current-drive-dominated* balance at the frozen operating point: the bootstrap term computed two ways, the drive mix sized to the honestly booked residual, and the whole answer stress-tested for its dependence on the one quantity — the bootstrap amplitude — that is not yet pinned by a full-profile kinetic run.

CONTRIBUTION

This paper contributes: (i) a formal derivation of the steady-state sustainment problem from the poloidal-flux diffusion equation down to the per-surface current balance (§2); (ii) an explicit evaluation of the neoclassical bootstrap current with both the Sauter closure and a first-principles NEO drift-kinetic calculation, including the collisionality dependence that makes the Sauter formula over-predict at low ν^* (§2, §4); (iii) the current-drive figure of merit and the mechanism trade among NBCD, ECCD and LHCD, with the accessibility and frequency gates written as inequalities (§2); (iv) a GPU-HPC computational methodology naming the actual codes run (§3); (v) results across eight data figures and six tables tracing every number to a register serial (§4); and (vi) a quantitative comparison to the published steady-state and current-drive literature (§5) together with a single, honestly stated open gate (§6). We cross-reference the companion papers of the Kronos 2026 series where they carry the adjacent physics: the neoclassical transport baseline [32], the negative-triangularity confinement that fixes the pressure profile [33,26,27], the heating-and-current-drive actuator systems [34], the solenoid-free startup and ramp [35], the poloidal-field coil set that shapes the equilibrium without a solenoid [36], the free-boundary equilibrium and MHD stability [37], the density-limit window [38], and the red-team margin study of current-drive headroom [39].

§ 2

Governing equations and the formal problem

THE POLOIDAL-FLUX (CURRENT) DIFFUSION EQUATION

Let ψ be the poloidal flux per radian and let ρ be a flux-surface label (we use the normalised toroidal flux). Ampère's law relates the flux-surface-averaged parallel current to the equilibrium metric, and Faraday's law plus the generalised parallel Ohm's law with neoclassical resistivity $\eta_{\parallel,\mathrm{neo}}$ and non-inductive sources gives the parallel force balance on the electrons,

$$\langle E\cdot B\rangle = \eta_{\parallel,\mathrm{neo}}\big(\langle j_\parallel B\rangle - \langle j_{\mathrm{bs}}\cdot B\rangle - \langle j_{\mathrm{cd}}\cdot B\rangle\big),$$

where $\langle\cdot\rangle$ is the flux-surface average, $\langle j_\parallel B\rangle$ the total parallel current, $\langle j_{\mathrm{bs}}\cdot B\rangle$ the bootstrap current, and $\langle j_{\mathrm{cd}}\cdot B\rangle = \sum_k \langle j_{\mathrm{cd},k}\cdot B\rangle$ the sum over external drive channels $k \in \{\mathrm{NB}, \mathrm{EC}, \mathrm{LH}\}$. Writing the inductive field as a time-changing poloidal flux, $\langle E\cdot B\rangle = -(\partial\psi/\partial t)\,\langle B\cdot\nabla\phi\rangle$, and inserting Ampère's law converts (1) into the one-dimensional current-diffusion equation [2,10,29,30]

$$\sigma_{\parallel,\mathrm{neo}}\,\frac{\partial\psi}{\partial t} = \frac{1}{\mu_0}\,\hat{\mathcal{L}}_\rho\,\psi + \frac{V'(\rho)}{2\pi}\,\frac{\langle j_{\mathrm{bs}}\cdot B\rangle + \langle j_{\mathrm{cd}}\cdot B\rangle}{\langle B^2\rangle^{1/2}},$$

with $\sigma_{\parallel,\mathrm{neo}} = 1/\eta_{\parallel,\mathrm{neo}}$ the neoclassical parallel conductivity, $V'(\rho) = \mathrm{d}V/\mathrm{d}\rho$ the differential volume, and $\hat{\mathcal{L}}_\rho$ the self-adjoint elliptic operator

$$\hat{\mathcal{L}}_\rho\,\psi = \frac{\partial}{\partial\rho}\left[g_2(\rho)\,\frac{\partial\psi}{\partial\rho}\right], \qquad g_2(\rho) = \left\langle \frac{|\nabla\rho|^2}{R^2}\right\rangle \frac{V'}{4\pi^2},$$

whose geometric coefficient g_2 is inherited from the Grad–Shafranov equilibrium and, for our strongly shaped negative-triangularity boundary, is supplied by the free-boundary solve of §3. Equation (2) is the transport equation for the current profile: the first term on the right diffuses the current resistively; the second is the non-inductive drive that, in steady state, must replace what resistive diffusion would otherwise require an inductive field to supply.

THE STEADY-STATE BALANCE

True steady state sets $\partial\psi/\partial t = 0$ and, with no sustained loop voltage, $\langle E\cdot B\rangle \to 0$. Equation (1) then collapses to a purely algebraic condition on every flux surface,

$$\boxed{\langle j_\parallel B\rangle = \langle j_{\mathrm{bs}}\cdot B\rangle + \sum_k \langle j_{\mathrm{cd},k}\cdot B\rangle}$$

i.e. the total current on each surface must be exactly the sum of the local bootstrap current and the locally driven current — there is no residual to be carried by induction. Integrating (4) over the poloidal cross-section gives the global constraint that organises the entire design,

$$I_p = I_{\mathrm{bs}} + \sum_k I_{\mathrm{cd},k}, \qquad 1 - f_{\mathrm{bs}} = \frac{1}{I_p}\sum_k I_{\mathrm{cd},k}, \qquad f_{\mathrm{bs}} \equiv \frac{I_{\mathrm{bs}}}{I_p}.$$

The smaller $1 - f_{\mathrm{bs}}$, the smaller the external drive bill; but the design does not get to choose f_{bs} freely — it is fixed by the pressure profile and the geometry through the neoclassical physics of the next subsection.

THE NEOCLASSICAL BOOTSTRAP CURRENT

The bootstrap current is the parallel return current carried by passing particles in response to the collisional friction against a trapped-particle population whose banana orbits sample the pressure gradient. In the Sauter–Angioni–Lin-Liu closure, valid at arbitrary collisionality, the flux-surface-averaged bootstrap current is [10,11]

$$\langle j_{\rm bs}\cdot \quad B\rangle = -I(\psi)\,p_e\left[\mathcal{L}_{31}\,\frac{\partial \ln p}{\partial\psi} + \mathcal{L}_{32}\,\frac{\partial \ln T_e}{\partial\psi} + \mathcal{L}_{34}\,\alpha\,\frac{1-R_{pe}}{R_{pe}}\,\frac{\partial \ln T_i}{\partial\psi}\right],$$

with $I(\psi) = RB_\phi$, electron pressure p_e, $R_{pe} = p_e/p$ the electron pressure fraction, α the ion-temperature-gradient coefficient, and the transport coefficients $\mathcal{L}_{31}, \mathcal{L}_{32}, \mathcal{L}_{34}$ functions of the effective trapped fraction and collisionality. The leading coefficient carries the essential structure,

$$\mathcal{L}_{31} = \left(1 + \tfrac{1.4}{Z+1}\right) f_{31} - \tfrac{1.9}{Z+1}\,f_{31}^2 + \tfrac{0.3}{Z+1}\,f_{31}^3 + \tfrac{0.2}{Z+1}\,f_{31}^4,$$

with the collisionality-reduced effective trapped fraction

$$f_{31} = \frac{f_t}{1 + (1-0.1 f_t)\sqrt{\nu_e^*} + 0.5\,(1-f_t)\,\nu_e^*/Z}, \qquad \nu_e^* = \frac{6.921\times10^{-18}\,R\,q\,n_e\,Z\,\ln\Lambda_e}{\varepsilon^{3/2}\,T_e^2},$$

(SI-practical units: n_e in m^{-3}, T_e in eV). The remaining coefficients $\mathcal{L}_{32}$ and $\mathcal{L}_{34}$ have the same rational-polynomial structure in f_t and ν^*. In the banana limit $\nu^* \to 0$ the effective trapped fraction $f_{31} \to f_t$, so the bootstrap current grows with f_t: the large trapped fraction of an ST is what makes each unit of β_p produce more bootstrap current. Two consequences matter for the present design. First, at our low collisionality ($\nu_e^* \simeq 0.012$, §4) the Sauter closure is known to slightly over-predict the current — the deep-banana regime is exactly where a first-principles operator differs, which is why we evaluate (6) against NEO. Second, combining (6) with the definition of β_p recovers the compact scaling

$$f_{\rm bs} \simeq c_{\rm bs}\,\sqrt{\varepsilon}\,\beta_p, \qquad \beta_p = \frac{\langle p\rangle}{B_\theta^2/2\mu_0},$$

which we use in §4 to explain why the ST value is modest.

TRAPPED FRACTION AND THE ST GEOMETRY

The effective trapped fraction is a flux-surface functional of the magnetic-field strength,

$$f_t = 1 - \frac{3}{4}\,\langle B^2\rangle \int_0^{1/B_{\rm max}} \frac{\lambda\,\mathrm{d}\lambda}{\langle\sqrt{1-\lambda B}\rangle},$$

which, for a circular-flux-surface local inverse aspect ratio $\varepsilon = r/R_0$, reduces to the standard engineering approximation

$$f_t \simeq 1 - \frac{(1-\varepsilon)^2}{\sqrt{1-\varepsilon^2}\,\left(1 + 1.46\sqrt{\varepsilon}\right)}.$$

At $A = 2.5$ ($\varepsilon = 0.40$ at the boundary) the ST sits at a much larger f_t than a conventional $\varepsilon \approx 0.1$ device on every surface; equation (11), evaluated at the local $\varepsilon(r) = (r/a)\,\varepsilon_{\rm edge}$, gives $f_t \simeq 0.60/0.65/0.70$ at $r/a = 0.5/0.6/0.7$ (§4, figure 7). The same large f_t reappears with opposite sign in the NBCD shielding correction below, so the ST geometry enters the current balance twice.

EXTERNAL CURRENT-DRIVE EFFICIENCY

An external actuator that deposits power density p_d and drives current density $j_\parallel$ has a local figure of merit $j_\parallel/p_d$. In the Fisch framework this is set by how efficiently the actuator pushes resonant electrons up in parallel velocity against collisional drag; in the high-velocity limit the dimensionless efficiency

$$\zeta \equiv \frac{j_\parallel/(e\,n_e v_{Te})}{p_d/(n_e T_e\,\nu_e)}$$

is an $O(1)$–$O(10)$ number that depends on the mechanism (Landau vs cyclotron vs beam) and on $Z_{\rm eff}$ [4,21]. Converting the local ratio to the engineering quantity a plant budgets — driven current per unit injected power — gives, in the conventional normalisation,

$$\gamma_{\mathrm{CD}} \equiv \frac{\bar{n}_{e,20}\, R_0\, I_{\mathrm{CD}}}{P_{\mathrm{CD}}} = C\,\zeta\,\frac{T_e}{5+Z_{\mathrm{eff}}},$$

with $\bar{n}_{e,20}$ the line-averaged density in $10^{20}\,\mathrm{m}^{-3}$, I_{CD} in amperes, P_{CD} in watts, and C a mechanism constant. Equation (13) exhibits the two hard levers: efficiency rises with electron temperature and falls with density and Z_{eff}. The frozen operating point fixes the aggregate. With $\bar{n}_{e,20} = 4.0$, $R_0 = 1.20\,m$, $I_{\mathrm{CD}} = 8.16\,MA$ supplied by $P_{\mathrm{CD}} = 118.5\,MW$,

$$\gamma_{\mathrm{eff}} = \frac{\bar{n}_{e,20}\, R_0\, I_{\mathrm{CD}}}{P_{\mathrm{CD}}} = \frac{4.0 \times 1.20 \times 8.16 \times 10^6}{118.5 \times 10^6} = 0.33 \times 10^{20}\ \mathrm{A\,W^{-1}\,m^{-2}},$$

a value squarely inside the range delivered by high-energy NBCD at conventional aspect ratio (§5).

THE DRIVE MIX: NBCD, ECCD, LHCD

The residual $8.16\,MA$ is carried by a mix chosen for efficiency, deposition location and controllability. Each channel comes with a physics gate.

Neutral-beam current drive. A fast ion born at energy E_b slows on electrons above, and on ions below, the critical energy

$$E_c = 14.8\, A_b\, T_e \left(\frac{1}{n_e} \sum_j \frac{n_j Z_j^2}{A_j} \right)^{2/3},$$

on the Spitzer slowing-down timescale $\tau_s = (3\sqrt{2\pi}\,\varepsilon_0^2 m_b T_e^{3/2})/(n_e e^4 m_e^{1/2} Z_b^2 \ln\Lambda)$; for our plasma $E_c \simeq 150\,keV$, so an energetic beam ($E_b \gg E_c$, negative-ion range) drives current efficiently and penetrates at $n_e = 4 \times 10^{20}\,\mathrm{m}^{-3}$. The net beam-driven current carries the trapped-electron shielding correction [17,18]

$$I_{\mathrm{NB}} = I_{\mathrm{NB}}^{(0)} \left[1 - \frac{Z_b}{Z_{\mathrm{eff}}} \big(1 - G(Z_{\mathrm{eff}}, \varepsilon)\big) \right],$$

in which the shielding term is *reduced* at large ε: the ST's large trapped fraction suppresses the electron back-current, so a compact ST is intrinsically favourable for NBCD. This is why the frozen design books the whole residual to NBCD as the workhorse.

Electron-cyclotron current drive. ECCD drives current by the Fisch–Boozer mechanism (selective heating of co-moving electrons) net of the Ohkawa counter-current (pitch-angle scattering into the trapped cone) [19,16]. Its deposition is set by the relativistic resonance

$$\omega = \frac{n\,\Omega_{ce}}{\gamma_L} = \frac{n\,eB}{\gamma_L m_e},$$

which localises the drive to the surface where the field matches the launched frequency. At $B_0 = 8\,T$ the fundamental is $f_{ce} \simeq 224$ Hertz *andthesecondharmonic*\simeq448, so ECCD here requires > 200 GHz gyrotrons; its role is not bulk current but precise, steerable profile control and tearing-mode suppression (companion actuator paper [34]).

Lower-hybrid current drive. LHCD is the most efficient channel per unit power, driving current by Landau damping on the fast-electron tail, but it must satisfy the accessibility condition on the launched parallel refractive index

$$n_\parallel > n_{\parallel,\mathrm{acc}} = \frac{\omega_{pe}}{\omega_{ce}} + \sqrt{1 + \frac{\omega_{pe}^2}{\omega_{ce}^2}}.$$

At our core parameters ($f_{pe} \simeq 180$ Hertz,f_ce\simeq224 , so $\omega_{pe}/\omega_{ce} \simeq 0.80$) equation (18) gives $n_{\parallel,\mathrm{acc}} \simeq 2.1$: the launched spectrum must sit above $n_\parallel \simeq 2.1$ to reach the plasma, and the corresponding Landau-resonant electrons live at $v_\parallel = c/n_\parallel$, which places the LH-driven current off-axis. LHCD is therefore booked as an off-axis current-profile actuator, gated by the high field and density, not as a core driver.

SOLENOID-FREE RAMP AND FLUX CONSUMPTION

Without a central solenoid the poloidal flux that links the plasma current must be self-generated by the driven and bootstrap current rather than supplied inductively. The flux linked is

$$\Psi_p = L_p I_p, \qquad L_p = \mu_0 R_0 \left[\ln \frac{8R_0}{a\sqrt{\kappa}} + \frac{\ell_i}{2} - 2 \right],$$

with ℓ_i the internal inductance; for the frozen geometry $L_p \simeq 2.03$ Henry, $giving$\Psi_p\simeq19.6 weber$. During ramp-up the current profile relaxes on the resistive redistribution (skin) time

$$\tau_R \sim \frac{\mu_0\, a^2\, \kappa}{2\, \eta_{\parallel,\mathrm{neo}}},$$

which for $\eta_{\parallel,\mathrm{neo}}$ at $T_e \sim 10\, keV$ is $\tau_R \simeq 14.5\, s$. Since the current must be built entirely by drive against this diffusion, the solenoid-free ramp to flat-top takes a few resistive times, $\tau_{\mathrm{ramp}} \simeq 43\, s$ (BR-CX-07); a schematic trajectory is $I_p(t) = I_p^{\mathrm{ft}}\,(1 - e^{-t/\tau_R})$. A flared ohmic-heating stack in the centrepost would restore inductive volt-seconds for the ramp phase alone, shortening it and cutting the seed-drive demand, but no such volt-seconds are required — or available — in the flat-top, where (4) holds identically.

§ 3

Computational methodology: the GPU HPC campaign

CODES AND THE CAMPAIGN

The numbers in this paper were produced on the Kronos NVIDIA GPU HPC campaign, on the same frozen configuration (config-22021) used across the breeder de-risking programme. Four solvers carry the current-sustainment problem. The neoclassical bootstrap current and conductivity are computed with the drift-kinetic code neo (GACODE) [14,15], build b493397, which solves the first-order drift-kinetic equation with the *full* linearised Fokker–Planck collision operator. The equilibrium geometry — the metric coefficient g_2 of equation (3) and the flux-surface averages of equations (10) — is supplied by a free-boundary Grad–Shafranov solve for the $\delta = -0.30$ boundary [37,36], with real-time equilibrium reconstruction in the EFIT lineage [25]. The kinetic pressure profile that drives the bootstrap term is set by flux-driven integrated transport with tgyro/tglf (register BR-L1-A11, $\tau_E \simeq 0.410\,s$, $H_{98} \simeq 0.94$) and cross-checked against nonlinear cgyro turbulence [22,33]. The Sauter closure of equations (6)–(8) is evaluated by the kronos_toolkit bootstrap module as a fast surrogate. All runs carry the campaign seed 20260726.

DRIFT-KINETIC DISCRETIZATION AND CONVERGENCE

neo solves for the first-order distribution f_1 on each flux surface from

$$v_{\parallel}\,\nabla_{\parallel} f_1 + \quad v_d\cdot\nabla f_0 = C[f_1],$$

where f_0 is a local Maxwellian, v_d the magnetic drift, and $C[\cdot]$ the full linearised multi-species Fokker–Planck operator (COLLISION_MODEL=4). The velocity space is expanded spectrally: a Legendre series in pitch angle $\xi = v_{\parallel}/v$ (N_XI=17), a Laguerre-type energy discretization (N_ENERGY=8), and a poloidal grid (N_THETA=25) around the flux surface, with a Miller local-equilibrium parameterisation (EQUILIBRIUM_MODEL=2) at $R_0/a = 2.5$, $\kappa = 2.0$, $\delta = -0.30$ (with a linear triangularity profile $S_\delta = -0.3\,\rho$), Shafranov shift -0.10, and kinetic electrons. The bootstrap current is the first parallel velocity moment of the converged f_1,

$$\langle j_{\mathrm{bs}}\cdot \quad B\rangle = \sum_s e_s \int v_{\parallel}\, f_{1,s}\, \mathrm{d}^3 v.$$

The physical normalisation uses $B_{\mathrm{unit}} \simeq B_0\kappa = 16\,T$ and the sound speed c_s, so the code output $\langle j_{\parallel} B\rangle / B_{\mathrm{unit}}$ is reported both in the dimensionless $e\,n_e c_s$ units native to the solver and in $\mathrm{MA\,m^{-2}}$. Convergence was confirmed by refinement in N_XI and N_ENERGY: the reported parallel current is stable to better than the $\sim 16\%$ NEO/Sauter difference it is used to resolve.

GPU ACCELERATION, SCALE AND REPRODUCIBILITY

Three radial surfaces ($r/a = 0.5, 0.6, 0.7$), each at its physical collisionality, were run concurrently on the NVIDIA GPU fleet, with the field-particle collision matrix assembly and the sparse drift-kinetic solve carried on the GPUs; the analytic Sauter surrogate, the toolkit current balance, and the inductance/resistive-time reduction of equations (19)–(20) run on the in-house node. This split lets the expensive first-principles operator and the fast design-space surrogate share one frozen configuration. Every input deck, the neo build hash, and the derived current-balance quantities are archived under the register serials so that a third party can regenerate table 3 and figures 2–3 byte-for-byte; no compute-cost information is part of the public record.

QUANTITY	SYMBOL	VALUE
plasma current	I_p	9.66 MA
fusion gain / power	Q / P_{fus}	3.076 / 85.04 MW
major / minor radius	R_0 / a	1.20 m / 0.48 m
aspect ratio ($\varepsilon = 0.40$)	$A = R_0/a$	2.5
elongation / triangularity	κ / δ	2.0 / −0.30
on-axis / centrepost field	B_0 / B_{cp}	8 T / 16.84 T

table continued

edge safety factor	q_{95}	3.0
line density	$\bar{n}_e$	$4.0 \times 10^{20}\ \mathrm{m}^{-3}$ ($f_G = 0.3$)
ion temperature (axis)	T_{i0}	15 keV
energy confinement	τ_E	0.410 s ($H_{98} \simeq 0.94$)

§ 4

Results

THE CURRENT BALANCE

Figure 1 and table 2 state the result that organises the design. Of the $9.66\,MA$ total, the pressure-driven bootstrap current self-supplies $1.50\,MA$ ($f_{\mathrm{bs}} = 0.155$) and external non-inductive drive supplies the remaining $8.16\,MA$. The device is therefore *current-drive-dominated*: 84.5% of the current is externally sustained. This is the opposite of a high-β_p steady-state reactor, in which bootstrap alignment is the central problem; here, with f_{bs} small, the safety-factor profile is fixed mainly by the external deposition and the load-bearing constraint is drive power.

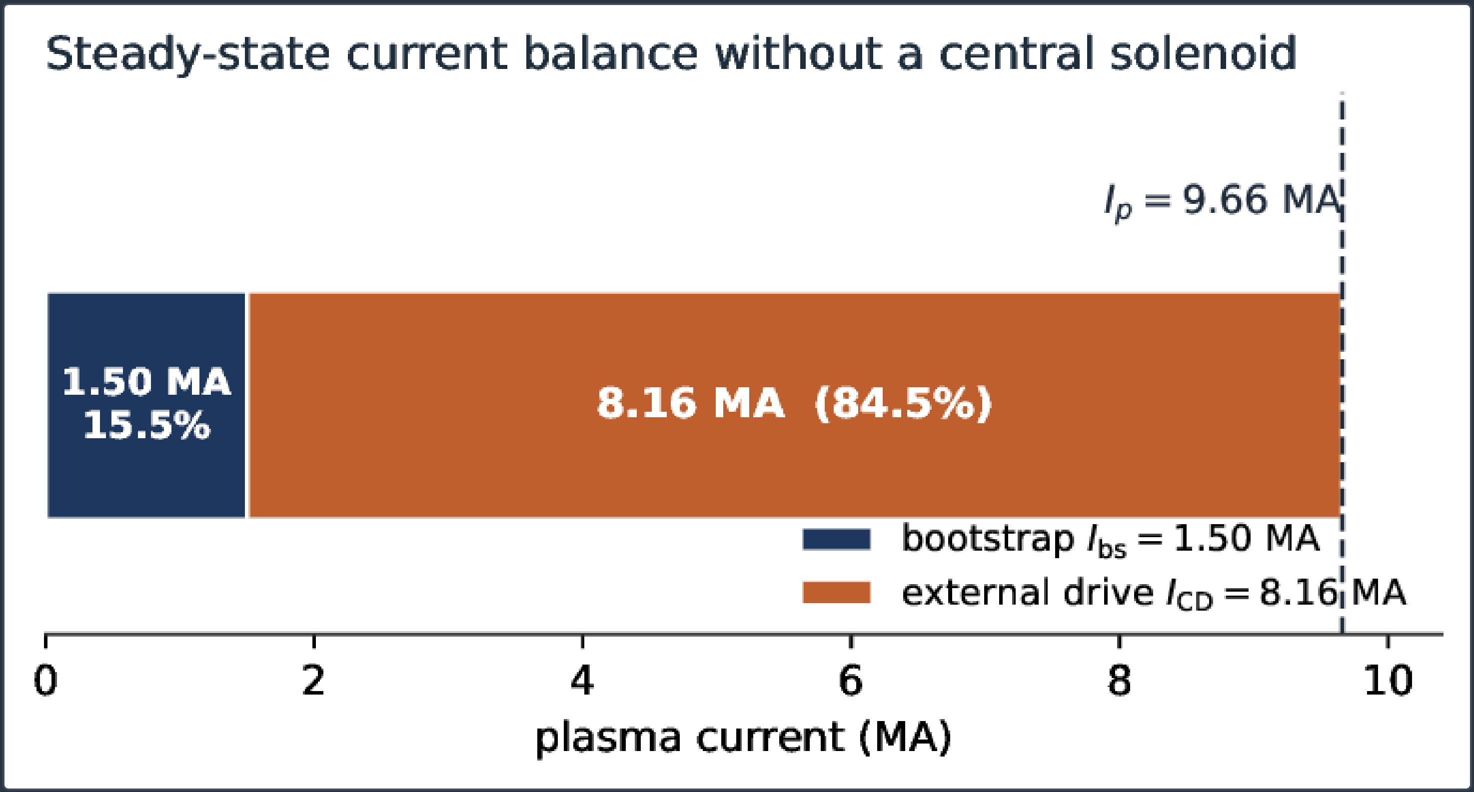

Steady-state current balance at the frozen operating point (BR-L2-A6, BR-CX-07): of the $9.66\,MA$ plasma current, $1.50\,MA$ (15.5%) is self-generated bootstrap and $8.16\,MA$ is external non-inductive drive. The device is current-drive-dominated.

QUANTITY	SYMBOL	VALUE
total plasma current	I_p	9.66 MA
bootstrap current	I_{bs}	1.50 MA
externally driven current	I_{cd}	8.16 MA
bootstrap fraction	f_{bs}	0.155
bootstrap-fraction band	$[f_{\mathrm{bs}}]$	[0.164, 0.282]
aggregate drive efficiency	γ_{eff}	$0.33 \times 10^{20}\ \mathrm{A\,W^{-1}\,m^{-2}}$
booked drive power	P_{CD}	118.5 MW (NBCD)

Global current balance, equation (5) (BR-L2-A6, BR-CX-07). The bounds are the toolkit range for peaked-pressure profiles.

FIRST-PRINCIPLES BOOTSTRAP CURRENT: NEO VERSUS SAUTER

Figure 2 shows the bootstrap current-density profile computed by the NEO drift-kinetic solver and by the Sauter closure at three flux surfaces, and table 3 tabulates them. The two agree in shape and to within $\simeq 16\%$ in magnitude, with NEO systematically *below* Sauter: the NEO/Sauter ratio is $0.811/0.843/0.873$ at $r/a = 0.5/0.6/0.7$. This is the expected physics, not a discrepancy: at the operating collisionality $\nu_e^* \simeq 0.012$ the plasma is deep in the banana regime, where the Sauter fit is known to over-predict, and a first-principles collision operator recovers the reduction (figure 3, left). The right panel of figure 3 compares closures at $r/a = 0.6$: the Koh and modified-Sauter models cluster near the Sauter value, NEO sits $\simeq 16\%$ lower, and the banana-limit-only Hirshman–Hinton estimate is far below, confirming that the collisionality treatment — not the geometry — controls the spread. The physical current densities are modest, $\langle j_\parallel B\rangle/B_{\text{unit}} \simeq 0.34/0.45/0.59$ MA m^{-2} (NEO), consistent with the low poloidal beta.

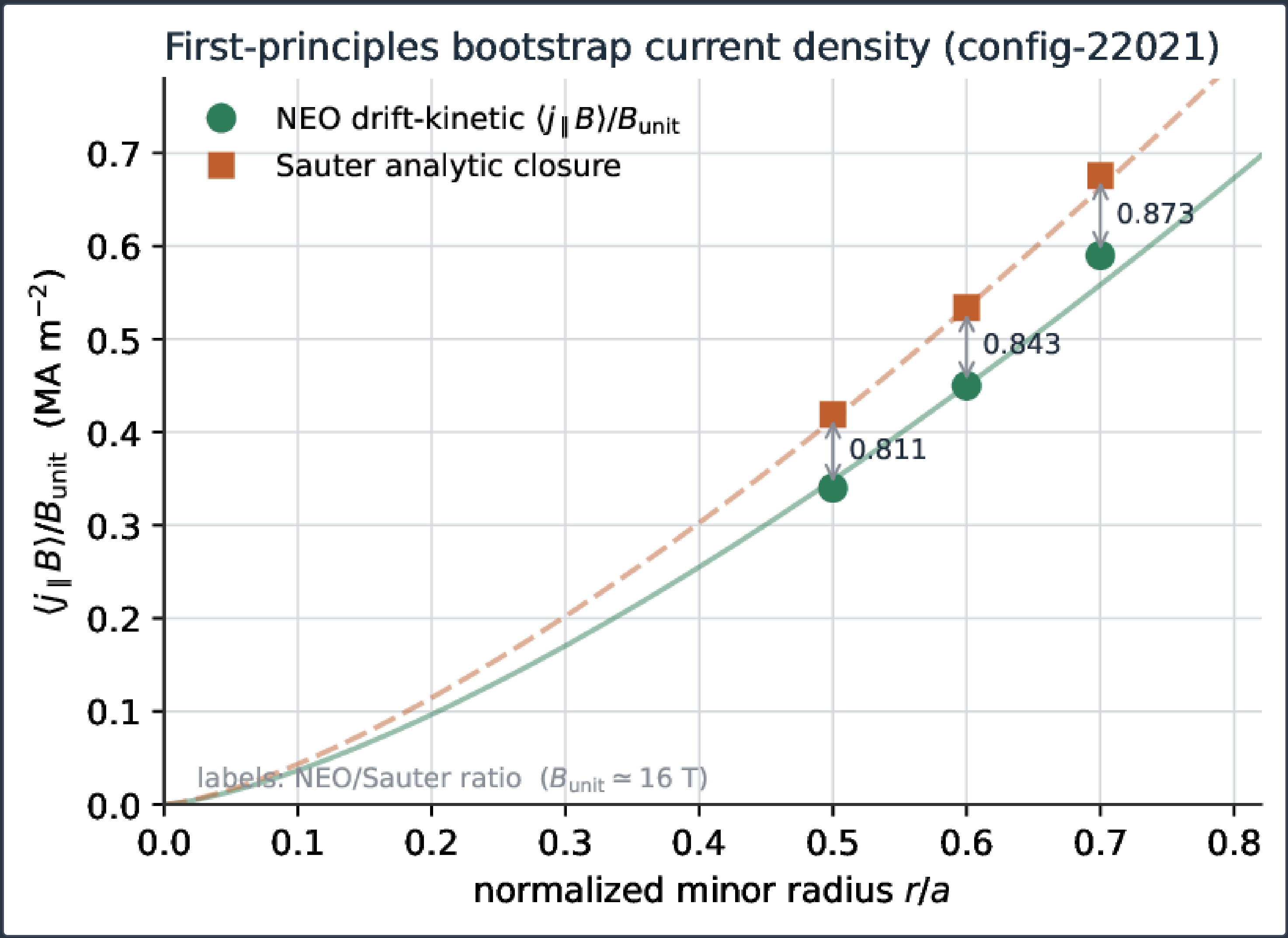

Bootstrap current density $\langle j_\parallel B\rangle/B_{\text{unit}}$ versus normalised radius (BR-L2-A16): NEO drift-kinetic (circles) and the Sauter closure (squares), with the NEO/Sauter ratio labelled at each surface. $B_{\text{unit}} \simeq 16\,T$. Curves are monotone guides through the three anchored points.

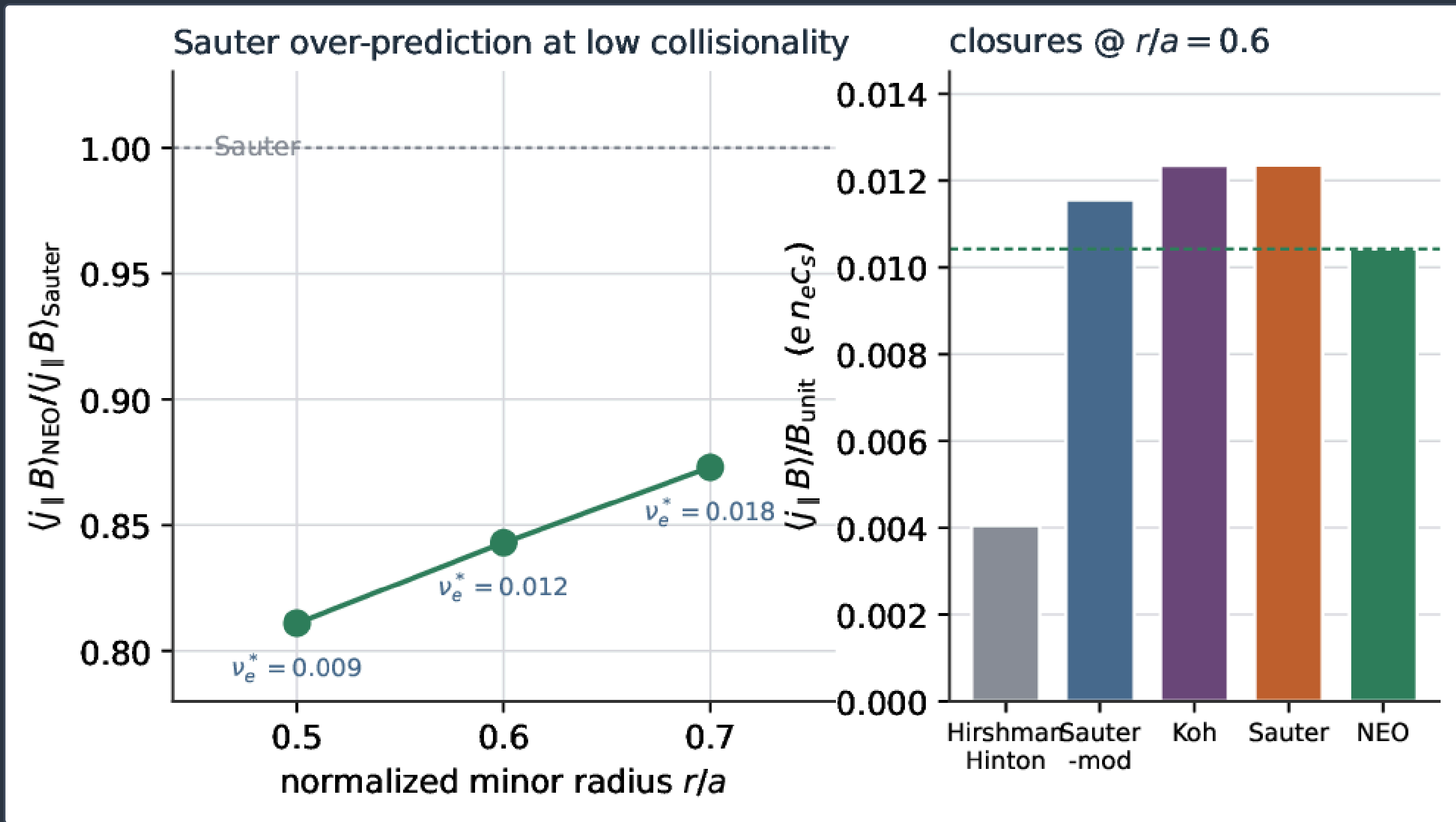

Left: the NEO/Sauter parallel-bootstrap ratio versus radius, annotated with the electron collisionality ν_e^*; all three surfaces sit in the banana regime where Sauter over-predicts. *Right:* alternate neoclassical closures at $r/a = 0.6$ in native $e\,n_e c_s$ units — Hirshman–Hinton (banana limit only), modified Sauter, Koh, Sauter, and NEO (dashed line). (BR-L2-A16.)

r/a	ν_e^*	$\langle j_\parallel B\rangle/B_{\rm unit}$ NEO	$\langle j_\parallel B\rangle/B_{\rm unit}$ SAUTER	NEO/SAUTER
		(MA m^{-2})	(MA m^{-2})	
0.5	~0.009	0.34	0.42	0.811
0.6	0.012	0.45	0.53	0.843
0.7	~0.018	0.59	0.68	0.873

First-principles bootstrap current by flux surface (BR-L2-A16; NEO build b493397, full Fokker–Planck). Physical densities from $\langle j_\parallel B\rangle/B_{\rm unit}$ with $B_ unit§I16

THE DRIVE MIX AND THE EFFECTIVE EFFICIENCY

Figure 4 plots the current-drive figure of merit of the three mechanisms against electron temperature, each following equation (13) with its mechanism constant, and marks the aggregate frozen point $\gamma_{\rm eff} = 0.33 \times 10^{20}\ \mathrm{A\,W^{-1}\,m^{-2}}$ of equation (14). Table 4 sets out the roles: NBCD is the on-axis workhorse (favoured in the ST by the reduced trapped-electron shielding of equation (16)), ECCD is the localised profile-control and tearing-suppression actuator gated by the $>200\,\mathrm{GHz}$ resonance of equation (17), and LHCD is the off-axis high-efficiency channel gated by the $n_{\parallel,\rm acc} \simeq 2.1$ accessibility of equation (18). The frozen design books the whole residual to NBCD at $118.5\,MW$; the RF channels are held as profile-shaping and headroom actuators (companion [34,39]).

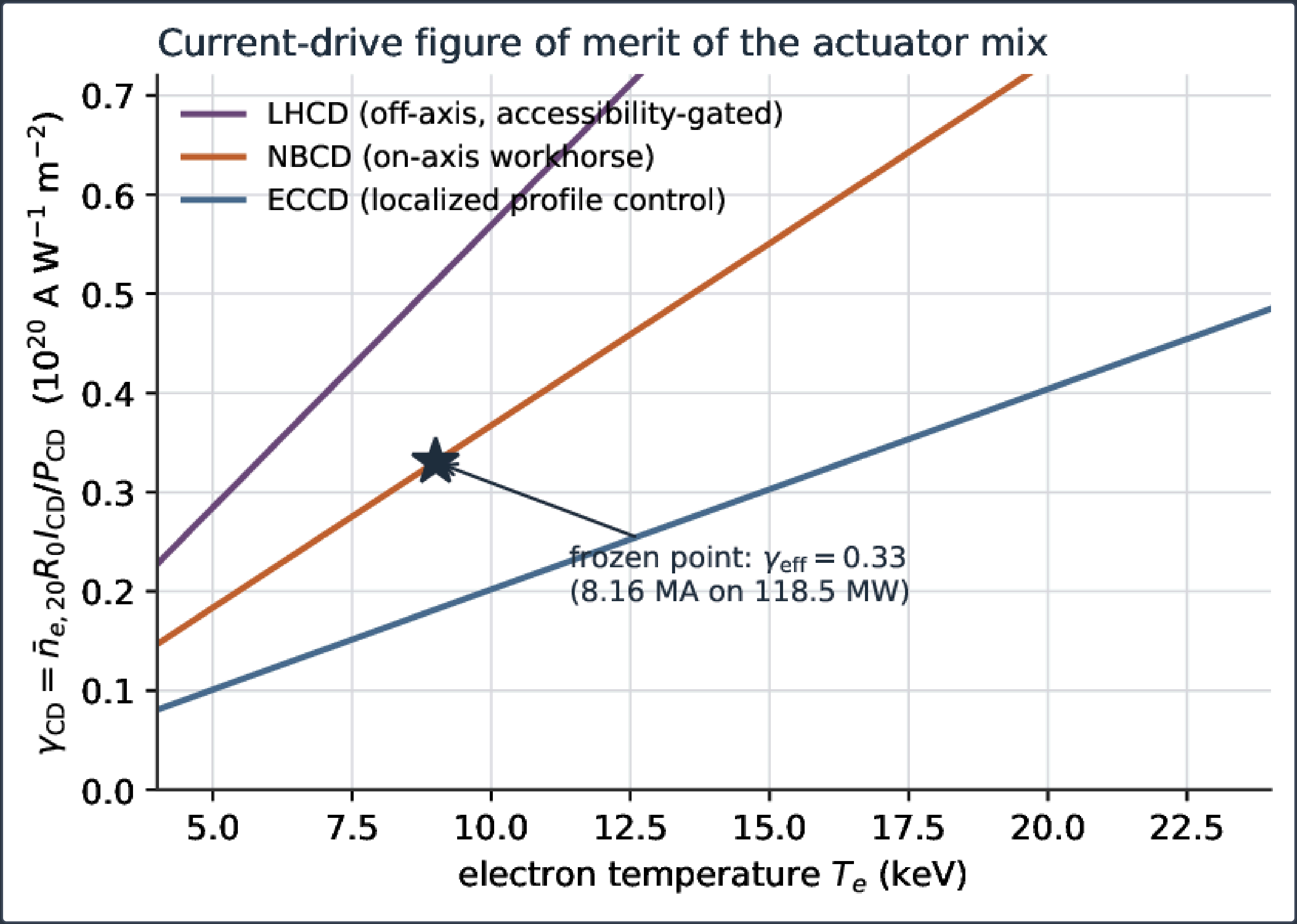

Current-drive figure of merit $\gamma_{\rm CD} = \bar{n}_{e,20} R_0 I_{\rm CD}/P_{\rm CD}$ versus T_e for the three mechanisms (equation (13); mechanism constants representative). The star marks the frozen aggregate $\gamma_{\rm eff} = 0.33$ implied by $8.16\,MA$ on $118.5\,MW$.

CHANNEL	$\gamma_{\rm CD}$ SCALING	DEPOSITION	ROLE	GATE
NBCD	$\propto T_e/(5+Z_{\rm eff})$; ST shield↓	broad, central	bulk current (workhorse)	$E_b \gg E_c \simeq 150\,keV$
ECCD	Fisch–Boozer – Ohkawa	narrow, steerable	q-profile / NTM control	$f_{ce} \simeq 224$ Hertz$
LHCD	highest ζ (Landau)	off-axis	off-axis current profile	$n_\parallel > n_{\parallel,\rm acc} \simeq 2.1$

The non-inductive drive mix, its scaling, deposition, role, and physics gate. Gates are equations (16), (17) and (18).

BOOTSTRAP-FRACTION SENSITIVITY AND A BOUNDED DRIVE BILL

Figure 5 propagates the bootstrap-fraction uncertainty into the drive power at fixed aggregate efficiency, $P_{\mathrm{CD}} = \bar{n}_{e,20} R_0 I_p (1 - f_{\mathrm{bs}})/\gamma_{\mathrm{eff}}$. The frozen point sits at $f_{\mathrm{bs}} = 0.155$, $P_{\mathrm{CD}} = 118.5\,MW$. The two bands mark the range the bootstrap amplitude might occupy: the crude full-profile NEO estimate ($f_{\mathrm{bs}} \simeq 0.075$–$0.087$, §6) on the low side, and the peaked-pressure toolkit band (0.164–0.282) on the high side. Across the *entire* plausible range the required drive power moves only between $\simeq 108\,MW$ and $\simeq 130\,MW$ — a $\sim 10\%$ swing about the booked value. Because the device is current-drive-dominated, the bootstrap magnitude is a second-order lever on the drive bill, never a first-order threat to sustainment. This is the quantitative reason the one open gate (§6) does not endanger the platform.

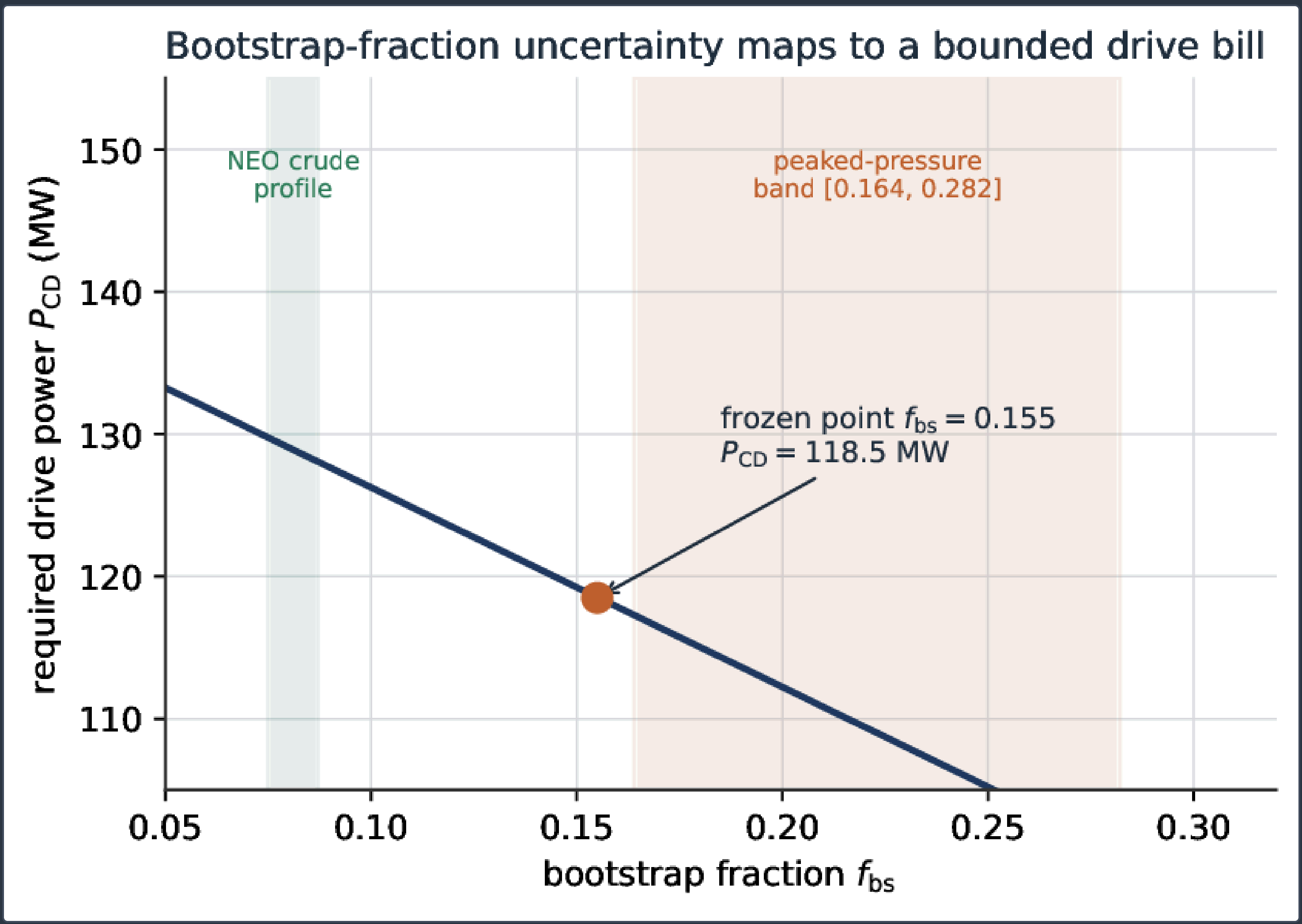

Required drive power versus bootstrap fraction at fixed γ_{eff} (BR-CX-07). Frozen point: circle. Shaded: the crude-NEO low band and the peaked-pressure high band. The whole span is a $\sim 10\%$ excursion in P_{CD}.

WHY THE ST BOOTSTRAP FRACTION IS MODEST

Figure 6 plots the scaling of equation (9). With $\varepsilon = 0.40$ ($\sqrt{\varepsilon} \simeq 0.63$) and $c_{bs} \simeq 1$, the operating point $f_{bs} = 0.155$ corresponds to $\beta_p \simeq 0.25$ — comfortably inside the Peng–Strickler ST regime of low poloidal beta ($\beta_p < 0.3$) [7]. The message is that the ST's large inverse aspect ratio, which enters f_{bs} through $\sqrt{\varepsilon}$, is offset by its intrinsically low β_p: the machine trades a high self-driven fraction for a high absolute current in a compact volume. The peaked-pressure band $[0.164, 0.282]$ corresponds to raising β_p by profile peaking; it does not change the qualitative regime.

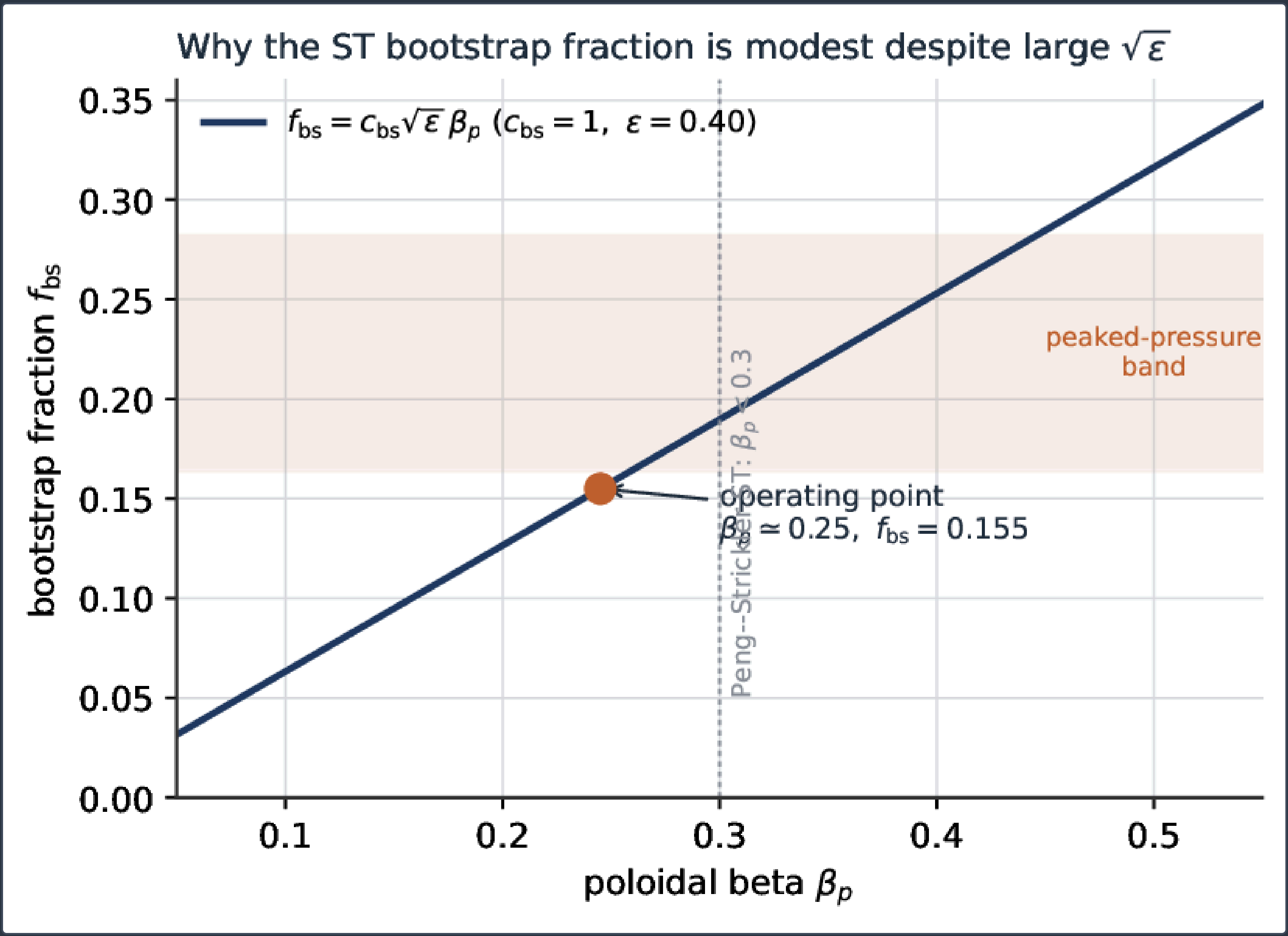

Bootstrap fraction versus poloidal beta, equation (9). The operating point ($\beta_p \simeq 0.25$, $f_{bs} = 0.155$) sits inside the low-β_p ST regime; the shaded band is the peaked-pressure range.

TRAPPED FRACTION AND THE ST GEOMETRY

Figure 7 evaluates equation (11). At the ST boundary ($\varepsilon = 0.40$) the trapped fraction is far above a conventional $\varepsilon \approx 0.1$ device on every surface, and at the mid-radius surfaces (local $\varepsilon = 0.20$–0.28) it reaches $f_t \simeq 0.60$–0.70. This large f_t is what boosts the bootstrap coefficients of equation (7) per unit β_p and, with opposite sign, suppresses the trapped-electron back-current in the NBCD shielding factor of equation (16) — so the same geometric feature helps the self-driven current and the beam-driven current at once.

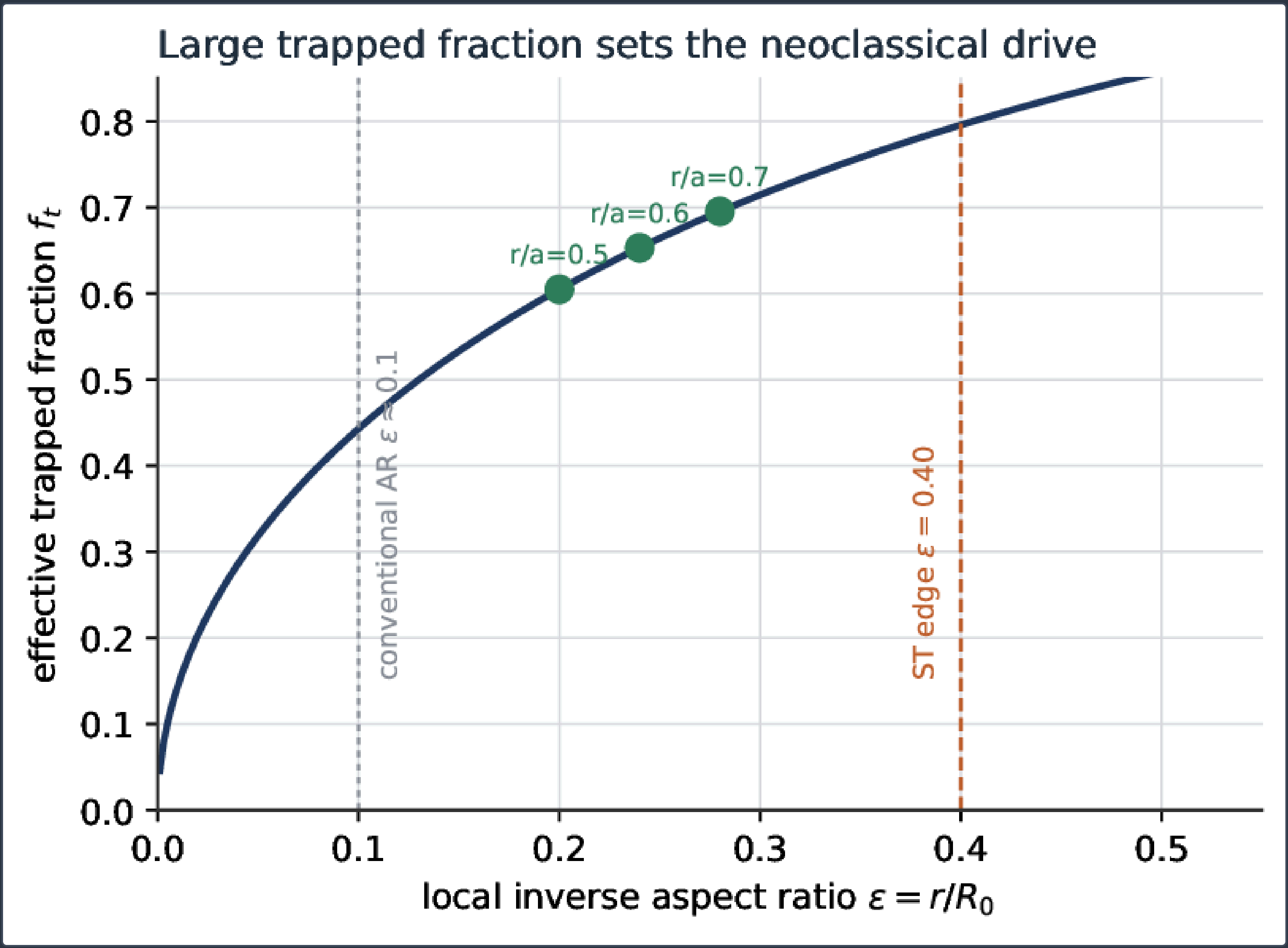

Effective trapped fraction versus local inverse aspect ratio, equation (11). Circles: the three flux surfaces at their local $\varepsilon = (r/a)\,\varepsilon_{\text{edge}}$. The ST edge ($\varepsilon = 0.40$) sits far above conventional aspect ratio.

THE SOLENOID-FREE RAMP

Figure 8 and table 5 give the ramp. The plasma links its own $\Psi_p \simeq 19.6\, weber$ of poloidal flux ($L_p \simeq 2.03$ Henry $) with no central solenoid, and the current - drive - limited ramp reaches flat - top in$\tau_ ramp\simeq43 s , $about three resistive redistribution times$(\tau_R\simeq14.5 s$). In flat-top the balance (4) holds with zero loop voltage. The detailed disruption-free ramp trajectory and the breakdown-to-flat-top access are treated in the startup companion [35]; here the point is that no inductive volt-seconds are required in steady state.

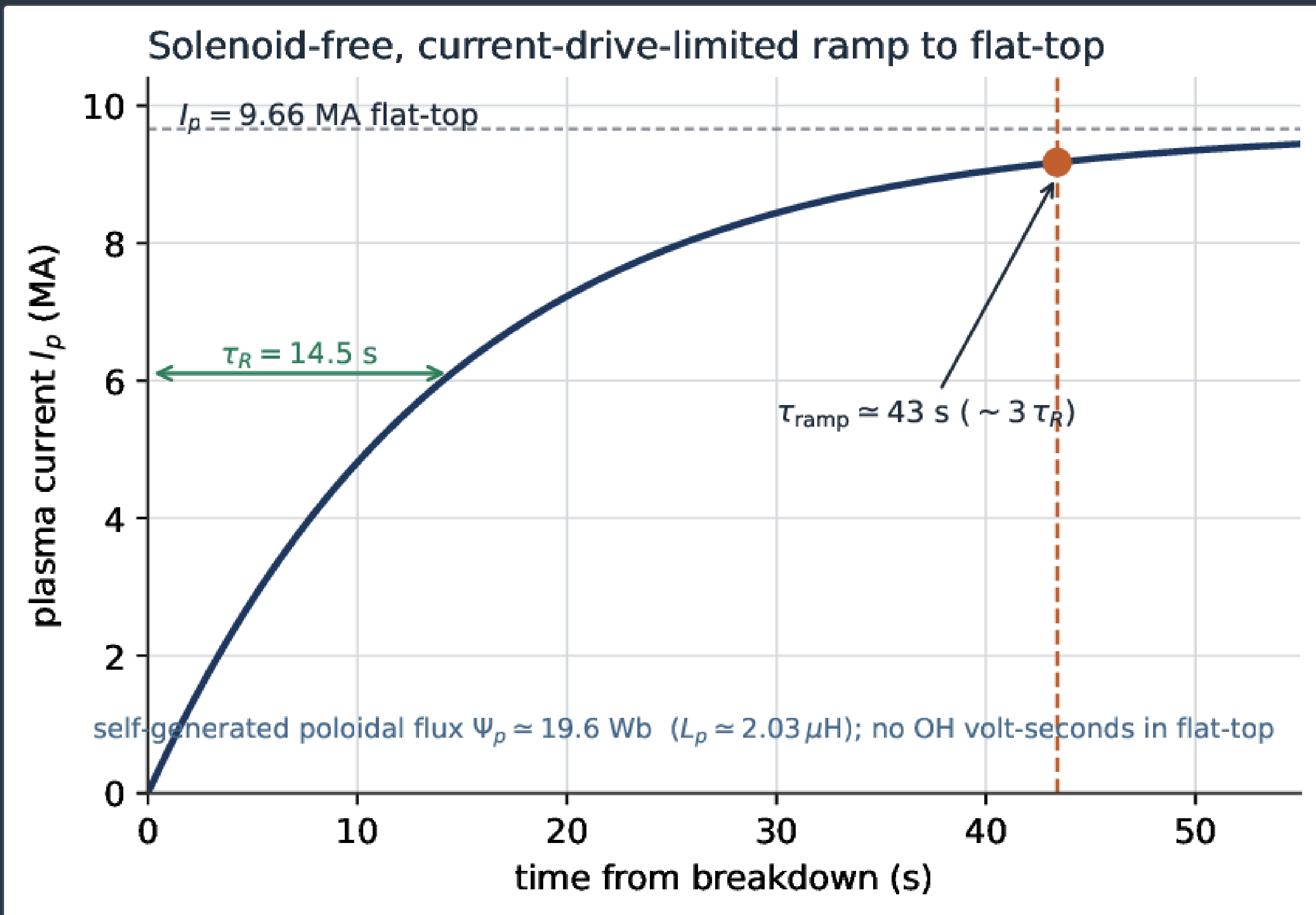

Solenoid-free, current-drive-limited ramp to the $9.66\, MA$ flat-top (BR-CX-07). The plasma self-generates $\Psi_p \simeq 19.6\, weber$; the ramp takes $\simeq 3\,\tau_R \simeq 43\, s$.

QUANTITY	SYMBOL	VALUE
plasma inductance	L_p	2.03 $Henry
self-generated poloidal flux	Ψ_p	19.6 weber
resistive redistribution time	τ_R	14.5 s
solenoid-free ramp time	τ_{ramp}	43.4 s
flat-top loop voltage	V_{loop}	0 (fully non-inductive)

Solenoid-free ramp and flux parameters, equations (19)–(20) (BR-CX-07).

DEPOSITION AND BOOTSTRAP ALIGNMENT

Figure 9 sketches how the mix aligns to a target current profile: the edge-weighted bootstrap current, the broad central NBCD, the localised ECCD, and the off-axis LHCD sum to the target $j_{\parallel}(r)$. Because f_{bs} is small, this alignment is comfortable — the external deposition sets the profile and the bootstrap is a minor, edge-weighted addition, rather than a large self-driven contribution the drive must be shaped around. The verification status of every quantity is collected in table 6.

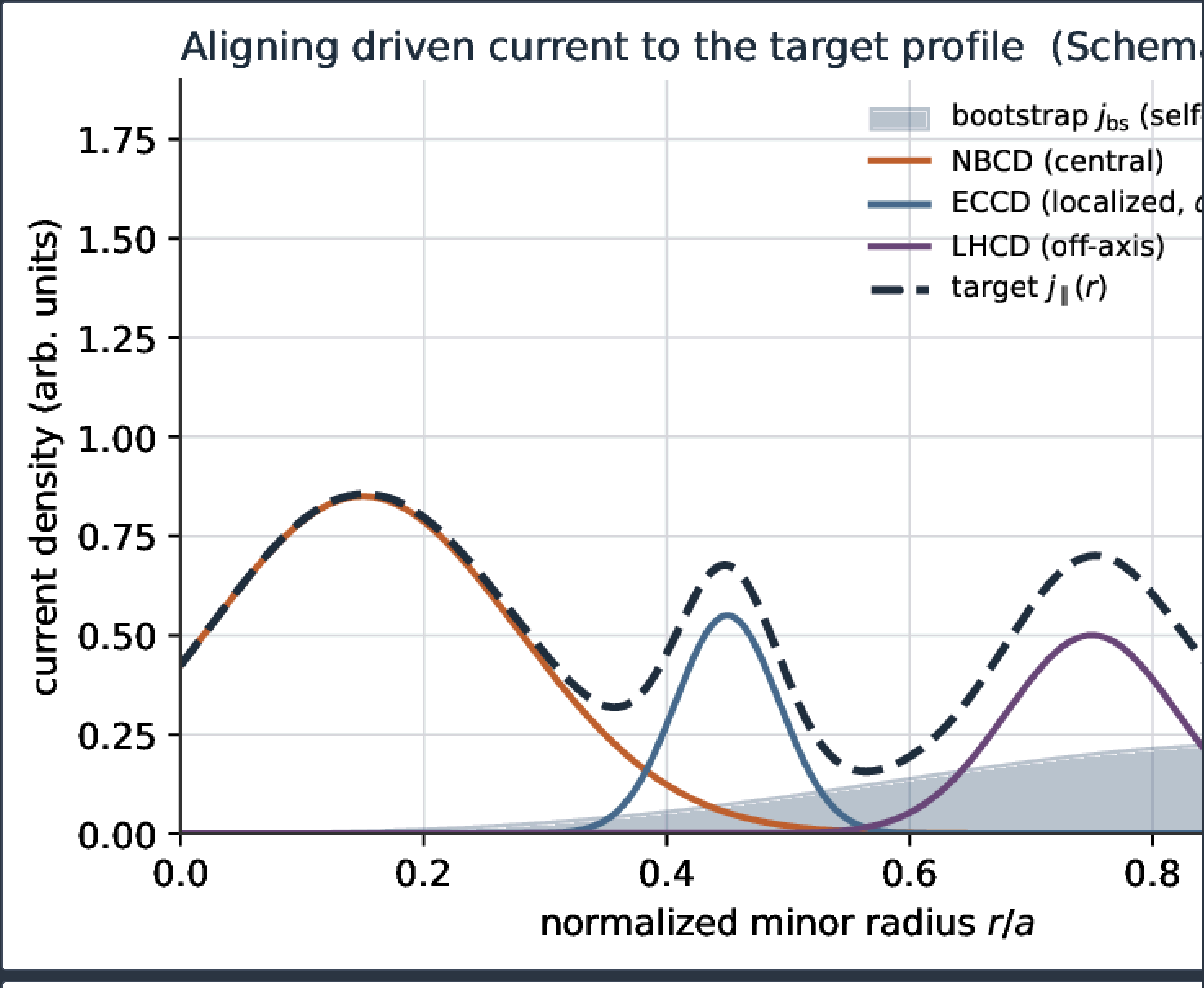
Aligning driven current to the target profile (Schem
bootstrap j_{bs} (self
NBCD (central)
ECCD (localized,
LHCD (off-axis)
target $j_\parallel(r)$
current density (arb. units)
1.75
1.50
1.25
1.00
0.75
0.50
0.25
0.00
0.0
0.2
0.4
0.6
0.8
normalized minor radius r/a

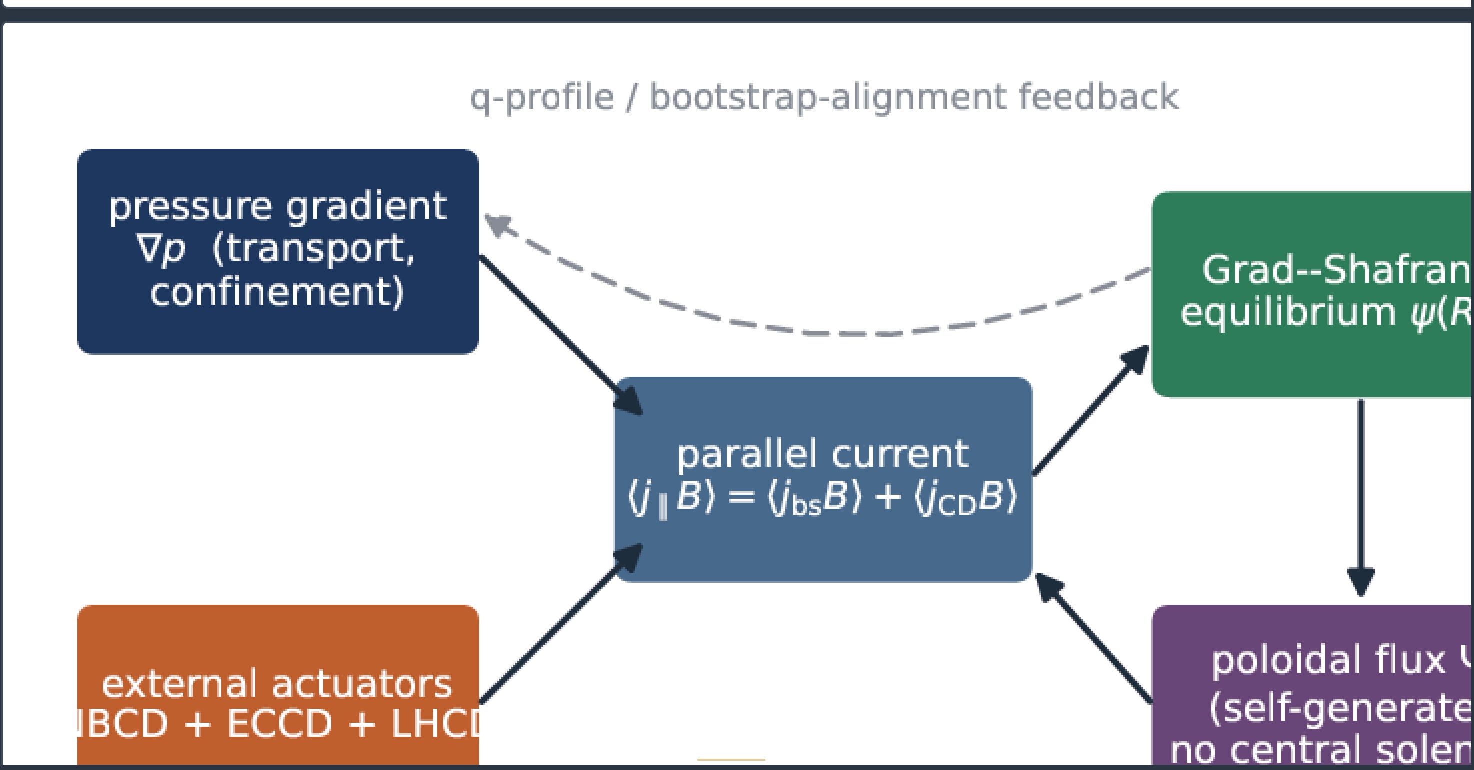
q-profile / bootstrap-alignment feedback
pressure gradient
∇p (transport, confinement)
Grad--Shafran
equilibrium $\psi(R$
parallel current
$\langle j_\parallel B\rangle = \langle j_{bs} B\rangle + \langle j_{CD} B\rangle$
external actuators
BCD + ECCD + LHCD
poloidal flux
(self-generate
no central solen

QUANTITY	VALUE	SERIAL	STATUS
design current, gain	9.66 MA, $Q{=}3.076$	BR-L1-A7	reproduced
bootstrap fraction (Sauter)	0.155	BR-L2-A6	reproduced
bootstrap NEO/Sauter ratio	0.81–0.87	BR-L2-A16	reproduced
current balance	$1.50 + 8.16$ MA	BR-CX-07	derived
solenoid-free ramp	$\Psi_p{\simeq}19.6$ Wb, $\tau_{\mathrm{ramp}}{\simeq}43$ s	BR-CX-07	derived
transport / confinement	$\tau_E{\simeq}0.410$ s, $H_{98}{\simeq}0.94$	BR-L1-A11	reproduced
bootstrap full-profile magnitude	open (see §6)	BR-L2-A16	flagged

Verification status of the current-sustainment quantities. Serials refer to the Kronos Physics De-Risking Register [31].

§ 5

Discussion

AGAINST THE STEADY-STATE REACTOR LITERATURE

The Hyperion balance is deliberately the mirror image of the classic high-β_p steady-state tokamak reactor. Kikuchi's SSTR concept operates at $\beta_p \gtrsim 2$ and $q \sim 4$–5 to drive up to 70% of the current by bootstrap, with the remainder from high-energy NBCD [9]; there, bootstrap *alignment* — matching the self-driven current profile to the equilibrium — is the central design problem, because the self-driven fraction is large. Hyperion instead runs at $\beta_p \simeq 0.25$ and $f_{\text{bs}} = 0.155$, so alignment is not the constraint: the external deposition sets the profile and the bootstrap is a minor addition. The compact ST reaches a large absolute current ($9.66\,MA$) in a small volume by paying for it in drive power rather than harvesting it from pressure. This is consistent with the Peng–Strickler ST scaling, which predicts low poloidal beta and large $I_p/(aB_0)$ for the spherical torus [7], and with the ST-FNSF/pilot-plant studies that similarly find compact STs to be current-drive-intensive [6].

THE BOOTSTRAP TERM AGAINST NEOCLASSICAL BENCHMARKS

The NEO/Sauter ratios of 0.81–0.87 we obtain are quantitatively in line with the known limitations of the Sauter fit. Redl *et al.* re-derived the neoclassical coefficients precisely because the original Sauter formulae lose accuracy at higher collisionality and with impurities [12], and kinetic edge studies find comparable corrections in steep-gradient regions [13]. Our operating surfaces sit deep in the banana regime ($\nu_e^* \simeq 0.012$), which is exactly where a first-principles collision operator returns a current below the banana-limit-anchored fit — the $\simeq 16\%$ reduction NEO reports is physics, not numerical disagreement. The banana-limit-only Hirshman–Hinton estimate, far below all the collisional models, confirms that the collisionality treatment dominates the closure spread [3].

THE DRIVE EFFICIENCY AGAINST CURRENT-DRIVE EXPERIENCE

The aggregate $\gamma_{\text{eff}} = 0.33 \times 10^{20}$ A W^{-1} m^{-2} that equation (14) extracts from the frozen point is squarely inside the envelope established for high-energy NBCD: the ITER Physics Basis and its steady-state chapter report NBCD efficiencies in the 0.2–0.4×10^{20} range for negative-ion beams at reactor temperature [5], and the ST's reduced trapped-electron shielding (equation (16)) works in our favour rather than against us. The RF channels bring complementary strengths: LHCD reaches the highest ζ but is accessibility-gated to off-axis deposition here (equation (18), $n_{\|,\text{acc}} \simeq 2.1$) [20], and ECCD, though modest in bulk efficiency, provides the steerable, localised authority for q-profile and tearing-mode control that a fully non-inductive discharge needs [19]. That authority is exercised by the real-time controllers of the companion control suite — both the classical shape and profile loops and the learned magnetic-control approaches now demonstrated on tokamaks [24] — and its headroom is stress-tested in the red-team study [39,34].

RELATION TO THE COMPANION PHYSICS

The pressure profile that fixes the bootstrap term is the negative-triangularity, ELM-free profile established by the confinement companion [33]; the collisional baseline beneath the bootstrap current is the neoclassical transport companion [32]; the equilibrium metric g_2 and the vertical-stability context come from the free-boundary equilibrium and PF-coil companions [37,36]; and the density that enters the drive efficiency through equation (13) is bounded by the Greenwald-fraction window ($f_G = 0.3$) [38]. The present paper is the current-sustainment node that ties these together into the closed balance of equation (4).

§ 6

Limitations

One gate is genuinely open. The bootstrap *amplitude* $f_{\rm bs} = 0.155$ is the Sauter/toolkit value; our first-principles NEO runs confirm the NEO/Sauter *ratio* (0.84 at mid-radius) but were performed at three local surfaces with a flat density profile ($\alpha_n = 0$, which removes the density-gradient drive) and with the $\langle j \cdot B \rangle / B_{\rm unit}$ output taken as the parallel current without full flux-surface and geometry correction. A crude three-point profile integral of those local currents gives $f_{\rm bs} \simeq 0.075$–0.087, roughly a factor of two below 0.155. This is not a refutation of the Sauter value — the discrepancy is entirely within what the flat-density and geometry approximations of a local run can explain — but it means the bootstrap amplitude is not yet pinned by a faithful, full-profile drift-kinetic calculation with a real equilibrium (`PROFILE_MODEL=2`, proper $B_{\rm unit}$ and flux-surface integration). That calculation is the registered follow-on. Crucially, the platform does not hinge on its outcome: figure 5 shows that the entire plausible amplitude range, from 0.075 to 0.282, maps to only a $\sim 10\%$ change in the drive power, because the device is current-drive-dominated. The bootstrap magnitude is a lever on the recirculating-power bill, not a condition for sustainment.

§ 7

Conclusion

A continuously operating compact spherical-tokamak breeder sustains its $9.66\,MA$ current without a central solenoid by combining a modest, self-generated bootstrap current with a large external non-inductive drive. Starting from the poloidal-flux diffusion equation we reduced the problem to the per-surface balance $\langle j_{\|} B\rangle = \langle j_{\mathrm{bs}} \cdot \quad B\rangle + \langle j_{\mathrm{cd}} \cdot \quad B\rangle$ and its integral $I_p = I_{\mathrm{bs}} + \sum_k I_{\mathrm{cd},k}$, evaluated the bootstrap term with both the Sauter closure and a first-principles NEO drift-kinetic calculation (NEO/Sauter $= 0.81$–0.87, the expected low-collisionality reduction), and sized the drive: $1.50\,MA$ ($f_{\mathrm{bs}} = 0.155$) bootstrap and $8.16\,MA$ driven, booked at $118.5\,MW$ of NBCD for an aggregate efficiency $\gamma_{\mathrm{eff}} = 0.33 \times 10^{20}\ \mathrm{A\,W^{-1}\,m^{-2}}$. Because the device is current-drive-dominated, the one open item — a full-profile confirmation of the bootstrap amplitude — moves the drive power by only $\sim 10\%$ and never threatens sustainment. The plasma self-supplies its $\simeq 19.6\,weber$ of poloidal flux and reaches flat-top in $\simeq 43\,s$ with zero loop voltage. Every headline number is a frozen anchor in the Kronos Physics De-Risking Register; the drive bill is stated openly, as a steady-state design must.

Acknowledgments tocsectionAcknowledgments Part of the Kronos Fusion Energy 2026 design series. The authors thank the Kronos physics de-risking programme for the frozen result set underlying every quantitative claim, and the operators of the NVIDIA GPU HPC campaign on which the drift-kinetic and transport calculations were run.

Reproducibility. Every headline quantity is a frozen anchor in the Kronos Physics De-Risking Register [31] (doi:10.5281/zenodo.22133057): the bootstrap fraction (BR-L2-A6), the first-principles NEO/Sauter comparison (BR-L2-A16), the current balance and solenoid-free ramp (BR-CX-07), the design re-anchor (BR-L1-A7), and the transport baseline (BR-L1-A11). Each is regenerable from the archived input decks, the NEO build hash b493397, and the figure-generation script deposited with this paper; this paper is archived at doi:10.5281/zenodo.22645758; official version: https://www.kronosfusionenergy.com/publications/current-drive-and-bootstrap.html. No result depends on unpublished or proprietary data, and no economic content is part of the deposit.

Data availability tocsectionData availability The current-balance quantities, the NEO and Sauter bootstrap densities, and the derived ramp parameters used for figures 1–8 are archived with the deposit at doi:10.5281/zenodo.22645758 and trace to the register [31] by the serial identifiers cited inline. Any economic analysis is reported separately and is not part of the public deposit.

Competing interests tocsectionCompeting interests Provisional patent applications relating to aspects of this work have been filed.

tocsectionReferences

APPARATUS

Portfolio, People & Record

The intellectual-property estate, the people who built it, the limitations that gate it, and the sources it rests on.

1	4	40	27
GRANTED PATENT	2026 PROVISIONALS	TEAM MEMBERS	2022 PROVISIONALS

INTELLECTUAL PROPERTY

The patent portfolio

The estate spans a granted high-field magnet patent, pending utility and 2026 provisional filings that map to the two products, a digital-twin control provisional, a registered trademark application, and the original 2022 provisional family. Every patentable disclosure in the five-paper arXiv drop was protected **before** publication: the breeder and burner provisionals were filed 1–2 August, and a publication-gap omnibus filing the evening before the drop swept up the DEC, plasma-control, and REBCO-winding matter of the three otherwise-unprotected papers. Patent numbers and application serials are matters of public record; claim scope is summarised, not reproduced.

GRANTED & PENDING UTILITY

US 12,009,112	High-field tilted graded-REBCO magnet architecture (KRONO-002A) · *app. 17/878,550*	GRANTED
US 17/878,507	Core device / method (KRONO-001A) · *utility*	PENDING

2026 PROVISIONAL FILINGS — MAPPED TO THE PRODUCTS

64/124,209	Hyperion — spherical-tokamak tritium / helium-3 foundry · *breeder · filed Aug 2026*	FILED
64/124,220	Aegis / MetroVolt — synchrotron-cutoff, fuel-selection & plug-winding · *generator · filed Aug 2026*	FILED
64/115,167	KRONOS-CTRL digital-twin plant control · *provisional · filed Jul 2026*	FILED
64/005,440	Integrated spherical-tokamak fusion architecture · *early integrated-architecture filing · filed Mar 2026*	FILED
64/105,530	Negative-triangularity spherical-tokamak architecture · *foundational ST filing · filed Jul 2026*	FILED
64/128,097	Publication-gap omnibus — quasineutral two-species expander DEC · provenance-gated / latency-split plasma control · as-built high-field winding & conductor architecture · *filed 7 Aug 2026, the evening before the arXiv drop*	FILED

TRADEMARK & ORIGIN

FTK-98801894	Kronos Fusion Energy — trademark application	FILED
KR-2022-*	Original provisional family (KR-2022-00001 … 00027) · *27 filings, 2022*	PRIORITY

The narrow, defensible magnet novelty — the specific conductor and the digital-twin winding optimisation, not high-field REBCO as a category — is the commercial core that can earn ahead of any $Q > 1$ milestone, with markets in fusion magnet supply, MRI/NMR, accelerators, and proton therapy. The claim is scoped honestly: the high field is a *system field* result, not a stand-alone-coil record; the small-bore plug coil is structurally infeasible as a bare winding but resolved by a stress-managed structural shield (feasible-pending-FEA); and the winding-tape experiment returned a *null result*. The value is the method, not a field record.

THE TEAM

Founding partners, board, advisors & auditors

Kronos is built by a bench of advanced-fuel-fusion, high-field-magnet, direct-conversion, and materials specialists, with a board and operations team drawn from defense, national laboratories, and industry. Dates are shown as ranges; where a tenure has ended or is term-ending, the range says so.

FOUNDING PARTNERS — SCIENCE

Dr. Gerald Kulcinski
Co-Founder · Helium-3 & Advanced-Fuel Fusion
UW–Madison · 2023–Present

Dr. Carl Weggel
Chief Scientist / S.M.A.R.T. Design
MIT Alcator Program · 2022–Present

Dr. Robert J. Weggel
Magnetic Field Design
MIT Magnet Lab · 2022–Present

BOARD

Priyanca Ford
Founder & CEO · Executive Board
2022–Present

Bandel Carano
Finance / Strategy
Oak Investment Partners / Stanford · 2025–2026

Patrick Schweiger
Fusion Device Engineering
Oklo / CFS / TerraPower · 2025–Present

SCIENTIFIC ADVISORS

Dr. Steven O. Dean
Fusion Policy & History
DOE / Fusion Power Associates · 2025–Present

Dr. Patrick H. Diamond
Plasma Turbulence & Transport
UC San Diego · 2025–Present

Dr. Jack J. Dongarra
HPC & Numerical Algorithms
Turing Award · 2025–Present

Dr. Nasr M. Ghoniem
Chief Material Scientist
UCLA · 2025–Present

Dr. Siegfried Glenzer
Plasma Physics & Laser Fusion
Stanford / SLAC · 2022–Present

Dr. David A. Hammer
Pulsed-Power Fusion
Cornell · 2025–Present

Dr. Donald A. Spong
Plasma Theory & Confinement
ORNL · 2025–Present

Dr. Curtis Smith
Risk Assessment & Nuclear PRA
MIT / Idaho National Lab · 2025–Present

RADM (Ret.) David Goggins
Naval Engineering & Power-Plant Design
U.S. Navy · 2023–2026

Dr. Konstantin Batygin
Mathematician
Caltech · 2022–2025

Dr. Ruben Fair
Magnet Design / ITER Liaison
PPPL / Jefferson Lab · 2022–2025

Dr. Paul S. Weiss
Materials & Nanotechnology
UCLA · 2022–2025

SCIENTIFIC AUDITORS

Dr. Wilfred A. Cooper
Plasma Equilibrium Theory
EPFL / Swiss Plasma Center · 2025–Present

Dr. Ahmed Hassanein
Plasma–Material Interactions
Purdue / Argonne · 2025–Present

Dr. Patrick E. Hopkins
Extreme Thermal Materials
U. of Virginia · 2025–Present

Dr. Peter Hosemann
Materials Joining & Structural Integrity
UC Berkeley · 2025–Present

Dr. Travis W. Knight
Advanced Nuclear Fuels & Systems
U. of South Carolina · 2025–Present

Dr. Philippe Lebrun
Cryogenics & Magnet Cooling
CERN · 2025–Present

Dr. Nitendra Singh
Nuclear Safety & Fuel Cycle
ITER · 2025–Present

Dr. Guido Van Oost
Magnetic Confinement & Fusion Systems
Ghent University · 2025–Present

Dr. Gary S. Was
Radiation Materials & Structural Integrity
U. of Michigan · 2025–Present

Dr. Ray Sedwick
Direct Energy Conversion
U. of Maryland · 2025

OPERATIONS

Michael Laughlin
Chief Operating Officer
2022–Present

Martin Owens
Chief Strategy Officer
LANL / GE Hitachi · 2022–Present

MG (Ret.) Paul Pardew
Chief Contracting Officer
Army Contracting Command · 2022–Present

David Beck
Fusion Commercialization
U.S. Space Force · 2024–Present

Sushma Bhatia
Environmental & Legislative
Google · 2022–Present

Michael De Frenza
Technology Licensing
2023–Present

MG (Ret.) Robin L. Fontes
Cybersecurity & Defense
Army Cyber Command · 2022–Present

Vijay Gehani
Supply Chain & Components
INOX India · 2024–Present

Jon Michel Greenwood
IT & AI Infrastructure
Live Nation · 2023–Present

Brian C. O'Neill
National Security
CIA / ODNI · 2022–Present

Gen. (Ret.) Gustave F. Perna
DoD Liaison
Operation Warp Speed · 2022–2023

Andrea Romero
Marketing Lead
2022–Present

Legal counsel is retained; those roles are held on the internal roster and are not listed here.

SOURCES

References

1 A G Peeters, The bootstrap current and its consequences, *Plasma Phys. Control. Fusion* **42** B231 (2000). doi:10.1088/0741-3335/42/12B/318

2 F L Hinton and R D Hazeltine, Theory of plasma transport in toroidal confinement systems, *Rev. Mod. Phys.* **48** 239 (1976). doi:10.1103/RevModPhys.48.239

3 S P Hirshman and D J Sigmar, Neoclassical transport of impurities in tokamak plasmas, *Nucl. Fusion* **21** 1079 (1981).

4 N J Fisch, Theory of current drive in plasmas, *Rev. Mod. Phys.* **59** 175 (1987). doi:10.1103/RevModPhys.59.175

5 C Gormezano *et al*, Progress in the ITER Physics Basis, Chapter 6: Steady state operation, *Nucl. Fusion* **47** S285 (2007). doi:10.1088/0029-5515/47/6/S06

6 J E Menard *et al*, Fusion nuclear science facilities and pilot plants based on the spherical tokamak, *Nucl. Fusion* **56** 106023 (2016). doi:10.1088/0029-5515/56/10/106023

7 Y-K M Peng and D J Strickler, Features of spherical torus plasmas, *Nucl. Fusion* **26** 769 (1986). doi:10.1088/0029-5515/26/6/005

8 B N Sorbom *et al*, ARC: a compact, high-field, fusion nuclear science facility and demonstration power plant with demountable magnets, *Fusion Eng. Des.* **100** 378 (2015). doi:10.1016/j.fusengdes.2015.07.008

9 M Kikuchi, Steady state tokamak reactor based on the bootstrap current, *Nucl. Fusion* **30** 265 (1990). doi:10.1088/0029-5515/30/2/006

10 O Sauter, C Angioni and Y R Lin-Liu, Neoclassical conductivity and bootstrap current formulas for general axisymmetric equilibria and arbitrary collisionality regime, *Phys. Plasmas* **6** 2834 (1999). doi:10.1063/1.873240

11 O Sauter, C Angioni and Y R Lin-Liu, Erratum: Neoclassical conductivity and bootstrap current formulas [Phys. Plasmas 6, 2834 (1999)], *Phys. Plasmas* **9** 5140 (2002). doi:10.1063/1.1517052

12 A Redl, C Angioni, E Belli and O Sauter (ASDEX Upgrade Team and EUROfusion MST1 Team), A new set of analytical formulae for the computation of the bootstrap current and the neoclassical conductivity in tokamaks, *Phys. Plasmas* **28** 022502 (2021). doi:10.1063/5.0012664

13 S Koh, C S Chang, S Ku, J E Menard, H Weitzner and W Choe, Bootstrap current for the edge pedestal plasma in a diverted tokamak geometry, *Phys. Plasmas* **19** 072505 (2012). doi:10.1063/1.4736953

14 E A Belli and J Candy, Kinetic calculation of neoclassical transport including self-consistent electron and impurity dynamics, *Plasma Phys. Control. Fusion* **50** 095010 (2008).

15 E A Belli and J Candy, Full linearized Fokker–Planck collisions in neoclassical transport simulations, *Plasma Phys. Control. Fusion* **54** 015015 (2012). doi:10.1088/0741-3335/54/1/015015

16 N J Fisch and A H Boozer, Creating an asymmetric plasma resistivity with waves, *Phys. Rev. Lett.* **45** 720 (1980). doi:10.1103/PhysRevLett.45.720

17 Y R Lin-Liu and F L Hinton, Trapped electron correction to beam driven current in general tokamak equilibria, *Phys. Plasmas* **4** 4179 (1997).

18 D F H Start, J G Cordey and E M Jones, The effect of trapped electrons on beam driven currents in toroidal plasmas, *Plasma Phys.* **22** 303 (1980).

19 R Prater, Heating and current drive by electron cyclotron waves, *Phys. Plasmas* **11** 2349 (2004). doi:10.1063/1.1690762

20 P T Bonoli, Review of recent experimental and modeling progress in the lower hybrid range of frequencies at ITER relevant parameters, *Phys. Plasmas* **21** 061508 (2014). doi:10.1063/1.4884360

21 C F F Karney and N J Fisch, Efficiency of current drive by fast waves, *Phys. Fluids* **28** 116 (1985).

22 J Candy, E A Belli and R V Bravenec, A high-accuracy Eulerian gyrokinetic solver for collisional plasmas, *J. Comput. Phys.* **324** 73 (2016). doi:10.1016/j.jcp.2016.07.039

23 F Felici *et al*, Real-time physics-model-based simulation of the current density profile in tokamak plasmas, *Nucl. Fusion* **51** 083052 (2011). doi:10.1088/0029-5515/51/8/083052

24 J Degrave *et al*, Magnetic control of tokamak plasmas through deep reinforcement learning, *Nature* **602** 414 (2022). doi:10.1038/s41586-021-04301-9

25 L L Lao, H St John, R D Stambaugh, A G Kellman and W Pfeiffer, Reconstruction of current profile parameters and plasma shapes in tokamaks, *Nucl. Fusion* **25** 1611 (1985). doi:10.1088/0029-5515/25/11/007

26 A Marinoni, O Sauter and S Coda, A brief history of negative triangularity tokamak plasmas, *Rev. Mod. Plasma Phys.* **5** 6 (2021). doi:10.1007/s41614-021-00054-0

27 M E Austin *et al*, Achievement of reactor-relevant performance in negative triangularity shape in the DIII-D tokamak, *Phys. Rev. Lett.* **122** 115001 (2019). doi:10.1103/PhysRevLett.122.115001

28 A J Creely *et al*, Overview of the SPARC tokamak, *J. Plasma Phys.* **86** 865860502 (2020). doi:10.1017/S0022377820001257

29 J Wesson, *Tokamaks*, 4th ed., Oxford University Press (2011).

30 J P Freidberg, *Plasma Physics and Fusion Energy*, Cambridge University Press (2007).

31 P I Ford, *Kronos Physics De-Risking Register*, Kronos Fusion Energy 2026 series. doi:10.5281/zenodo.22133057

32 P I Ford and G L Kulcinski, Neoclassical transport, poloidal flows, and impurity screening in a compact spherical-tokamak breeder, Kronos 2026 series. doi:10.5281/zenodo.22645832

33 P I Ford and G L Kulcinski, Negative-triangularity turbulence suppression in a compact spherical-tokamak breeder, Kronos 2026 series. doi:10.5281/zenodo.22645722

34 P I Ford and G L Kulcinski, Heating and current-drive actuator systems for a compact spherical-tokamak breeder, Kronos 2026 series. doi:10.5281/zenodo.22645872

35 P I Ford and G L Kulcinski, From breakdown to flat-top: solenoid-free startup and disruption-free ramp access, Kronos 2026 series. doi:10.5281/zenodo.22645760

36 P I Ford, R J Weggel and C Weggel, Poloidal-field coil set and equilibrium-current optimization for a compact spherical-tokamak breeder, Kronos 2026 series. doi:10.5281/zenodo.22645945

37 P I Ford and G L Kulcinski, Free-boundary equilibrium and ideal-MHD stability of a compact spherical-tokamak breeder, Kronos 2026 series. doi:10.5281/zenodo.22645740

38 P I Ford and G L Kulcinski, The Greenwald-fraction density limit and the radiative boundary, Kronos 2026 series. doi:10.5281/zenodo.22645947

39 P I Ford, Red-teaming the frozen design point: current-drive and beta-headroom margins, Kronos 2026 series. doi:10.5281/zenodo.22645720

COLOPHON

How this document was made

The Kronos Fleet — Combined Editorial, 2026 is set in **Fraunces** (display), **Gelasio** (text), and **IBM Plex Mono** (data & equations), carried forward from the Kronos editorial design system.

The figures are rendered at 300 dpi from the deposited generator scripts; the document is composed as a single self-contained file with embedded fonts and imagery, paginated to US Letter, and rendered to PDF through a headless Chromium engine in matched light and dark editions.

Every headline quantity carries an evidence class; withdrawn and restated values are marked as such. Nothing herein is frozen beyond the founder-approved Tier-A set.

Explore it live — turn the interactive 3-D model, run the deposited solvers in the physics validator, and watch the companion film series.

LEGAL NOTICE

Notice, status, and distribution

Conceptual design & simulation study. This document reports a conceptual design and simulation study. It is not a construction commitment, a safety-analysis report, a regulatory filing, or an offer of securities. Forward-looking statements — schedules, costs, market sizes, and performance — are estimates subject to the limitations set out in the Simulations part and may change.

Numbers and their classes. Quantities are reported with evidence classes and case labels; modelled, assumed, and requirement-class values are identified as such and are not to be quoted without their labels.

Public edition. This edition carries the physics and design only; all financial, funding, and defense-commercial content has been removed for public distribution. The scientific text corresponds to the arXiv and journal submissions.

THE 2026 KRONOS SERIES

One programme, many papers

This editorial is one paper in the Kronos 2026 series — a real fusion company's complete, reproducible physics record for a spherical-tokamak breeder and its low-neutron D–^{3}He tandem-mirror burners. Every headline number is a frozen anchor in the Physics De-Risking Register.

Explore the whole programme: the De-Risking Register, the interactive 3-D model, and the physics validator.

KRONOS FUSION ENERGY

Bootstrap-Aligned Steady-State Current Sustainment Without a Central Solenoid: NBCD, ECCD and LHCD for a Compact Spherical-Tokamak Breeder

A real fusion company building real machines. Explore the science, live.

Zenodo · doi:10.5281/zenodo.22645758

Read on kronosfusionenergy.com

The Physics De-Risking Register